JCB Journal of Cell Biology

ARTICLE

The lysine catabolite saccharopine impairs development by disrupting mitochondrial homeostasis

Junxiang Zhou[1,2,3], Xin Wang[2], Min Wang[1], Yuwei Chang[4], Fengxia Zhang[4], Zhaonan Ban[3,4], Ruofeng Tang[1,3], Qiwen Gan[1,3], Shaohuan Wu[3,4,5], Ye Guo[1], Qian Zhang[1,3], Fengyang Wang[1,3], Liyuan Zhao[1,3], Yudong Jing[1], Wenfeng Qian[4,5], Guodong Wang[4], Weixiang Guo[1], and Chonglin Yang[1,2]

Amino acid catabolism is frequently executed in mitochondria; however, it is largely unknown how aberrant amino acid metabolism affects mitochondria. Here we report the requirement for mitochondrial saccharopine degradation in mitochondrial homeostasis and animal development. In *Caenorhbditis elegans*, mutations in the saccharopine dehydrogenase (SDH) domain of the bi-functional enzyme α-aminoadipic semialdehyde synthase AASS-1 greatly elevate the lysine catabolic intermediate saccharopine, which causes mitochondrial damage by disrupting mitochondrial dynamics, leading to reduced adult animal growth. In mice, failure of mitochondrial saccharopine oxidation causes lethal mitochondrial damage in the liver, leading to postnatal developmental retardation and death. Importantly, genetic inactivation of genes that raise the mitochondrial saccharopine precursors lysine and α-ketoglutarate strongly suppresses SDH mutation-induced saccharopine accumulation and mitochondrial abnormalities in *C. elegans*. Thus, adequate saccharopine catabolism is essential for mitochondrial homeostasis. Our study provides mechanistic and therapeutic insights for understanding and treating hyperlysinemia II (saccharopinuria), an aminoacidopathy with severe developmental defects.

Introduction

Mitochondria are central to cell metabolism by coordinating multiple catabolic and anabolic pathways and coupling the tricarboxylic acid cycle with ATP production via oxidative phosphorylation (Pagliarini and Rutter, 2013; Wai and Langer, 2016). In response to metabolic or developmental signals, mitochondria undergo dynamic fusion and fission, transport, and mitophagy, thus homeostatically maintaining their normal functions (Youle and van der Bliek, 2012; Mishra and Chan, 2016; Wai and Langer, 2016). Dysfunction or damage of mitochondria causes a wide spectrum of developmental or metabolic disorders (Pagliarini and Rutter, 2013; Mishra and Chan, 2016).

Amino acids are the building blocks of proteins. Additionally, they serve as an alternative energy supply within the cell. The degradation of amino acids is normally achieved by removal of the α-amino group followed by generation of various catabolic intermediates that participate directly or indirectly, depending on the type of amino acid, in the tricarboxylic acid cycle in mitochondria (Bruce Alberts, 2014). It is well known that disorders of amino acid metabolism often lead to aminoacidopathies with severe developmental defects, but the underlying pathological mechanisms are largely not understood. Particularly, whether aberrant amino acid catabolism exerts an adverse effect on mitochondrial structures and functions remains mostly obscure. In this study we explore this issue by investigating the requirement for lysine degradation in mitochondrial homeostasis in animals. Lysine is one of the essential amino acids for humans. If not used for protein synthesis, lysine is catabolized in mitochondria, where lysine and α-ketoglutarate are first converted into saccharopine, which is subsequently oxidized to α-aminoadipic semialdehyde. This ultimately leads to generation of acetyl-CoA that enters the tricarboxylic acid cycle (Markovitz et al., 1984; Papes et al., 1999; Sacksteder et al., 2000). Defective lysine catabolism leads to hyperlysinemia, an autosomal recessive metabolic disorder that can be grouped into two subtypes. While hyperlysinemia I exhibits a strong elevation in lysine in the blood or urine and is probably asymptomatic (Dancis et al., 1983),

---

[1]State Key Laboratory of Molecular Developmental Biology, Institute of Genetics and Developmental Biology, Chinese Academy of Sciences, Beijing, China; [2]State Key Laboratory of Natural Resource Conservation and Utilization in Yunnan and Center for Life Sciences, School of Life Sciences, Yunnan University, Kunming, China; [3]Graduate University of Chinese Academy of Sciences, Beijing, China; [4]State Key Laboratory of Plant Genomics, Institute of Genetics and Developmental Biology, Chinese Academy of Sciences, Beijing, China; [5]Key Laboratory of Genetic Network Biology, Institute of Genetics and Developmental Biology, Chinese Academy of Sciences, Beijing, China.

Correspondence to Chonglin Yang: clyang@genetics.ac.cn; Weixiang Guo: wxguo@genetics.ac.cn.

Rockefeller University Press
J. Cell Biol. 2019 Vol. 218 No. 2 580–597

https://doi.org/10.1083/jcb.201807204

hyperlysinemia II (also called saccharopinuria) is characterized by an abnormal increase in both lysine and saccharopine in the blood or urine, which might be associated with developmental retardation, intellectual disability, and spastic diplegia (Carson et al., 1968; Simell et al., 1972; Cederbaum et al., 1979; Cox et al., 1986; Vianey-Liaud et al., 1986; Houten et al., 2013). To date, it is not clear whether and how abnormal mitochondrial lysine catabolism may affect mitochondrial dynamics and functions. In addition, it is not known if mitochondrial dysfunction contributes to either subtype of hyperlysinemia. Here we uncover the requirement for complete saccharopine catabolism to maintain mitochondrial homeostasis, and we provide a mechanistic basis to distinguish the asymptomatic hyperlysinemia I from the detrimental saccharopinuria.

Results

Mutations in *aass-1* cause abnormal mitochondrial enlargement in *Caenorhbditis elegans*

To investigate the mechanisms underlying mitochondrial homeostasis, we generated a *C. elegans* strain carrying an integrated array (*yqIs157*) that specifically expresses mitochondrion-targeted GFPs (Mito-GFPs) in hypodermal cells, which are large and flat and thus convenient for microscopic study of mitochondria. In WT (N2) animals carrying *yqIs157*, Mito-GFP–labeled mitochondria predominantly exhibit tubular morphology through developmental larval stages 2 (L2) to 4 and in adult animals (Fig. 1 A). We then performed ethyl methanesulfonate (EMS) mutagenesis of *yqIs157*-carrying N2 worms to screen for mutants that display abnormal mitochondrial morphology. Among the mutants we identified, *yq170* and *yq211* similarly accumulated greatly enlarged spherical structures positive for Mito-GFP through larval developmental stages, and these structures became more predominant and evenly distributed in hypodermal cells at the adult stage (Fig. 1, A and B). Using the integrated array *hqIs181*, which expresses GFP tagged with the mitochondrial localization sequence (mtLS::GFP) in multiple tissues, we also observed abnormally enlarged mtLS::GFP structures in adult gonad sheath cells but not in intestinal or muscle cells in *yq170* mutants (Fig. 1, C–E). To confirm the mitochondrial identity of the Mito-GFP–positive abnormal structures, we used mCherry-tagged TOMM-20 (TOMM-20::mCh; outer mitochondrial membrane) and GFP-tagged IMMT-1 (IMMT-1::GFP; inner mitochondrial membrane) to label mitochondria in the hypodermis. Compared with the predominantly tubular mitochondria in N2 animals, TOMM-20::mCh- and IMMT-1::GFP-positive mitochondria were spherical and greatly enlarged in *yq170* mutants (Fig. 1 F). The TOMM-20::mCh- or Mito-GFP–labeled enlarged mitochondria did not colocalize with either autophagosomes, which were marked with GFP-tagged LGG-1 (GFP::LGG-1), the *C. elegans* homologue of LC3/Atg8, or lysosomes, which were labeled with the lysosomal DNase II NUC-1 tagged with mCherry (NUC-1::mCh; Fig. S1, A and B). In addition, other intracellular organelles including autophagosomes, lysosomes, endosomes, the Golgi apparatus, and the ER in *yq170* mutants were indistinguishable from those in N2 animals (Fig. S1, A–C). These results together demonstrate that the *yq170* and *yq211* mutations specifically caused abnormal enlargement of mitochondria in hypodermal cells. *yq170* and *yq211* failed to complement one another, suggesting that they affected the same gene.

We mapped *yq170* and *yq211* to linkage group (LG) IV and found that they affected the *R02D3.1* gene. *R02D3.1* encodes an orthologue of human α-aminoadipate semialdehyde synthase (AASS), which degrades lysine in mitochondria (Papes et al., 1999; Sacksteder et al., 2000). *R02D3.1* was thus renamed *aass-1* (Fig. 1, G–I). Within the *aass-1* gene, *yq170* and *yq211* changed nucleotide 5484 from C to T and nucleotide 4775 from G to A, respectively, leading to the mutations S641F and G499E in the encoded protein (Fig. 1, G and H). Transgenic expression of mCherry-fused AASS-1 (AASS-1::mCh) driven by the *aass-1* promoter ($P_{aass\text{-}1}$*aass-1::mCh*) revealed that the AASS-1 fusion protein localized to mitochondria and fully rescued the abnormal mitochondrial morphology in *aass-1(yq170)* mutants (Fig. S1, D and G). In addition, GFP driven by the *aass-1* promoter ($P_{aass\text{-}1}$*GFP*) was expressed in hypodermal cells from embryonic to adult stages, and in adult gonad sheath cells, but not in intestinal and muscle cells (Fig. S1, E and F). Consistent with this, AASS-1::mCh driven by the promoter of the hypodermal cell-specific gene *Y37A1B.5*, but not the promoters of the intestine-specific *vha-6* gene and the muscle-specific *myo-3* gene, rescued the abnormal mitochondrial morphology of *aass-1(yq170)* mutants (Fig. S1 G). These results suggest that the hypodermis is the tissue where AASS-1 is expressed and plays a functional role. Collectively, these results show that *yq170* and *yq211* are mutations of the *aass-1* gene that cause abnormal enlargement of mitochondria in the hypodermis.

Only mutations in the SDH domain of AASS-1 induce mitochondrial abnormality

Human AASS is a mitochondrial protein comprised of two enzymes, the N-terminal lysine-ketoglutarate reductase (LKR) and the C-terminal saccharopine dehydrogenase (SDH; Fig. 1 H; Sacksteder et al., 2000). LKR first catalyzes the conversion of lysine and α-ketoglutarate to saccharopine, and SDH subsequently oxidizes saccharopine to generate glutamate and α-aminoadipate semialdehyde (Fig. 1 I). This leads to degradation of lysine in mitochondria (Sacksteder et al., 2000). Because the *yq170* and *yq211* mutations both occur in SDH in *C. elegans* AASS-1, we investigated whether additional *aass-1* mutants available in WormBase and the *Caenorhabditis* Genetics Center that affect either SDH or LKR had similar mitochondrial enlargement. The *gk328753* mutation, which results in a G666D mutation in SDH, led to mitochondrial enlargement like the *yq170* and *yq211* mutations (Fig. 2, A, B, and D). In contrast, mutations affecting only LKR, *gk652575* (G150R) and *gk533395* (P217S), did not change the mitochondrial morphology compared with WT (Fig. 2, A, B, and D). The premature termination mutation *gk650376* (W159 to stop), which affects both LKR and SDH, did not change the mitochondrial morphology either (Fig. 2, A, B, and D). In addition, the *ok926* deletion mutant, in which the C-terminal part of LKR and the whole SDH are deleted, did not have abnormal mitochondria (Fig. 2, A, B, and D). These findings indicate that the abnormal mitochondrial enlargement was dependent on an intact LKR together with mutations that specifically inactivate SDH. Supporting

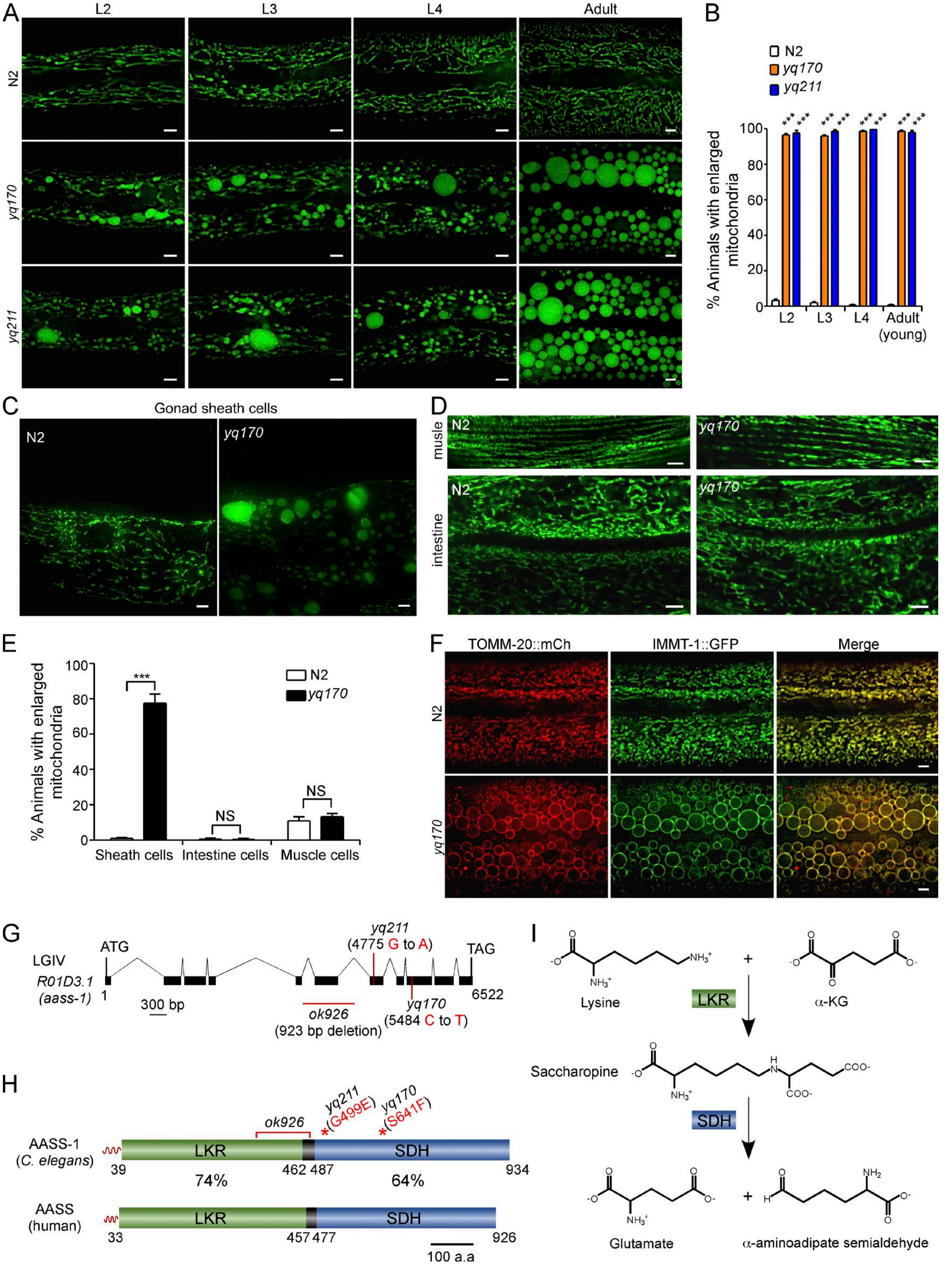

Figure 1. **Mutations in *aass-1* cause abnormal mitochondrial enlargement in *C. elegans*. (A)** Representative images of Mito-GFP–labeled structures in the hypodermis of N2, *yq170*, and *yq211* animals carrying *yqIs157* at the indicated developmental stages. Bars, 5 µm. **(B)** Quantification of animals with abnormally enlarged mitochondria (area ≥12 µm^2) as shown in A. 90 animals or more were scored for each genotype. Comparisons are between N2 and mutants. **(C and D)** Images of mtLS::GFP-labeled structures in gonad sheath cells (C) and muscle and intestinal cells (D) in the indicated animals carrying *hqIs181*. Bars, 5 µm. **(E)** Quantification of animals with an abnormally enlarged mitochondria (area ≥12 µm^2) as shown in C and D. 90 animals or more were scored for each genotype. **(F)** Images of mitochondria labeled with TOMM-20::mCh and IMMT-1::GFP in the hypodermis of animals with the indicated genotypes. Bars, 5 µm. **(G)** Schematic representation of the *aass-1* gene. Filled boxes represent exons, and thin lines indicate introns. The *ok926* deletion and point mutations of *aass-1* are indicated with red lines. **(H)** Comparison of *C. elegans* AASS-1 with human AASS. The wavy lines represent mitochondrial targeting sequences (MTSs). The deletion and point mutations in AASS-1 are indicated with a red line and asterisks, respectively. **(I)** Graphic description of mitochondrial lysine degradation. α-KG, α-ketoglutarate. For all quantifications, *, $P < 0.05$; **, $P < 0.01$; and ***, $P < 0.001$. Error bars represent SEM.

this conclusion, inactivation of *aass-1* by RNAi did not induce any mitochondrial abnormality; instead, it suppressed the abnormal mitochondrial enlargement in *aass-1(yq170)* mutants (Fig. 2, C and D). Moreover, transgenic expression of mitochondrion-targeted, mCherry-tagged LKR (MTS::LKR::mCh) failed to rescue the enlargement of mitochondria in *aass-1(yq170)* mutants. However, expression of a similarly tagged SDH (MTS::SDH::mCh), but not SDH containing the *yq170* (S641F) or *yq211* (G499E) mutations, strongly rescued the mitochondrial defects in *yq170* mutants (Fig. 2, E–H and J). SDH::mCh that was not targeted to mitochondria did not rescue the defective mitochondria in *yq170* mutants either (Fig. 2, I and J). Taken together, these results suggest that mitochondrial activity of SDH is required for maintenance of the normal morphology of mitochondria.

Saccharopine accumulation causes mitochondrial damage and impairs adult growth

Mutations in SDH likely cause accumulation of saccharopine, which in turn induces abnormal enlargement of mitochondria (Fig. 1 I). To investigate this possibility, we examined saccharopine and lysine levels in N2, *aass-1(yq170)* mutants, and *aass-1(yq211)* mutants. N2 animals had very low levels of saccharopine (0.362 ± 0.037 µmol/g; Fig. S1 H). However, saccharopine levels were greatly increased by >150-fold in *aass-1(yq170)* (59.212 ± 0.072 µmol/g) and *aass-1(yq211)* (53.711 ± 1.807 µmol/g) mutants (Figs. 3 A and S1 H). Lysine levels were much higher than saccharopine levels in N2 animals (Fig. S1 H). Interestingly, lysine levels were further increased by 3–4-fold in *aass-1(yq170)* and *aass-1(yq211)* mutants compared with the WT (Figs. 3 B and S1 H), which probably results from feedback inhibition of LKR by saccharopine (Fig. 1 I; Pink et al., 2011). *aass-1(ok296)* deletion mutants, which are deficient in both LKR and SDH, exhibited normal mitochondrial morphology and had a very low level of saccharopine like N2 animals, but the lysine levels were increased as in *aass-1(yq170)* and *aass-1(yq211)* SDH mutants (Fig. 3, A and B; and Fig. S1 H). These data suggest that the strong increase in mitochondrial saccharopine, rather than lysine, is responsible for the abnormal mitochondrial enlargement in *aass-1(yq170)* and *aass-1(yq211)* SDH mutants. To corroborate this conclusion, we sought to reduce the mitochondrial import of lysine by inactivating the mitochondrial lysine importer. RNAi depletion of *slc-25A29*, which encodes a homologue of the mammalian mitochondrial basic amino acid importer SLC25A29 (Porcelli et al., 2014), strongly suppressed the abnormal mitochondrial enlargement in *aass-1(yq170)* mutants (Fig. S2, A and B). Using a CRISPR/Cas9-based method (Jinek et al., 2012; Cong et al., 2013; Mali et al., 2013), we generated the *slc-25A29(yq276)* mutant, which contains a premature mutation in the *slc-25A29* gene (Fig. S2, C and D). The lysine concentration in *aass-1(yq170);slc-25A29(yq276)* double mutants remained at a high level, similar to that in *aass-1(yq170)* single mutants; however, the saccharopine levels in the double mutants were greatly reduced (Fig. 3, A and B; and Fig. S1 H). Like *slc-25A29* RNAi, *slc-25A29(yq276)* did not induce abnormal mitochondria (Fig. 3 C). Moreover, double mutants of *slc-25A29(yq276)* with *aass-1(yq170)* exhibited normal mitochondrial morphology, like N2 animals (Fig. 3 C). Thus, blocking mitochondrial import of lysine greatly decreased the generation of saccharopine and consequently inhibited saccharopine-induced abnormal mitochondrial enlargement in *aass-1* SDH mutants.

Next, we examined the mitochondrial ultrastructure by transmission electron microscopy (TEM). TEM revealed that mitochondria in N2 hypodermis had predominantly tubular or small spherical morphologies, similar to those detected with fluorescent markers (Fig. 3 D). In contrast, *aass-1(yq170)* mutants mainly contained greatly enlarged and spherical mitochondria in hypodermal and gonad sheath cells, but not in muscle or intestinal cells (Figs. 3 D and S3 A). Remarkably, the cristae in these enlarged mitochondria were severely damaged, and the membranes of many mitochondria were broken (Fig. 3 D). 3D reconstruction of randomly picked mitochondria ($n = 4$) indicated that they were indeed leaky (Fig. 3 E and Videos 1 and 2). In addition, we found that some abnormally enlarged mitochondria were tightly connected, suggesting that they were probably undergoing fusion (Fig. 3 D). The enlarged and broken mitochondria in *aass-1(yq170)* hypodermis were distinct from those in the *tm1133* deletion mutants of *fzo-1*, which encodes the *C. elegans* homologue of mammalian MFN1/2 required for fusion of mitochondrial outer membranes. In *fzo-1(tm1133)* mutants, mitochondria were small and spherical with no obvious cristae. These mitochondria contained internal membranes, and the outer membranes were intact (Fig. S3 B). In *aass-1(ok926)* deletion mutants and *aass-1(yq170);slc-25A29(yq276)* double mutants, however, mitochondrial morphologies and structures appeared similar to those in N2 animals (Fig. 3 D). Given that saccharopine levels in these single and double mutants were greatly reduced but lysine levels remained as high as in *aass-1(yq170)* single mutants, these TEM results confirmed the conclusion that accumulation of saccharopine caused abnormal mitochondrial enlargement and damage.

We next assessed the function of mitochondria in *aass-1* mutants. Using a luciferase-based ATP measurement assay (de Wet et al., 1987; Lagido et al., 2001, 2008), we found that *aass-1(yq170)* and *aass-1(yq211)* mutant hypodermis, but not intestine, had greatly reduced ATP levels compared with WT (Figs. 3 F and S3 C). Staining with Mito-CMXROS, a dye for mitochondrial membrane potential, indicated that mitochondria lost their membrane potential in *aass-1(yq170)* and *aass-1(yq211)* hypodermis (Figs. 3 G and S3 D). The generation of mitochondrial reactive oxygen species, measured using a cpYFP probe (Shen et al., 2014; Xu and Chisholm, 2014), was also strongly reduced (Figs. 3 H and S3 E). Thus, saccharopine accumulation induced by SDH mutations led to mitochondrial damage and consequently functional loss.

Interestingly, *aass-1(yq170)*, *aass-1(yq211)*, and *aass-1(ok926)* mutants had a similar life span to N2 animals (Fig. 3 I), suggesting that saccharopine-induced mitochondrial damage in the hypodermis did not affect life span. However, the body lengths of *aass-1(yq170)* and *aass-1(yq211)* adult animals were significantly shorter than the WT, as revealed by a time-course measurement of animals after the L4 stage (Fig. 3 J). Transgenic expression of mitochondrion-targeted SDH in *aass-1(yq170)* mutants successfully rescued their body lengths to WT levels (Fig. 3 J). Importantly, *aass-1(ok926)* deletion mutants and *aass-1(yq170);slc25A-29(yq276)* double mutants, which had no

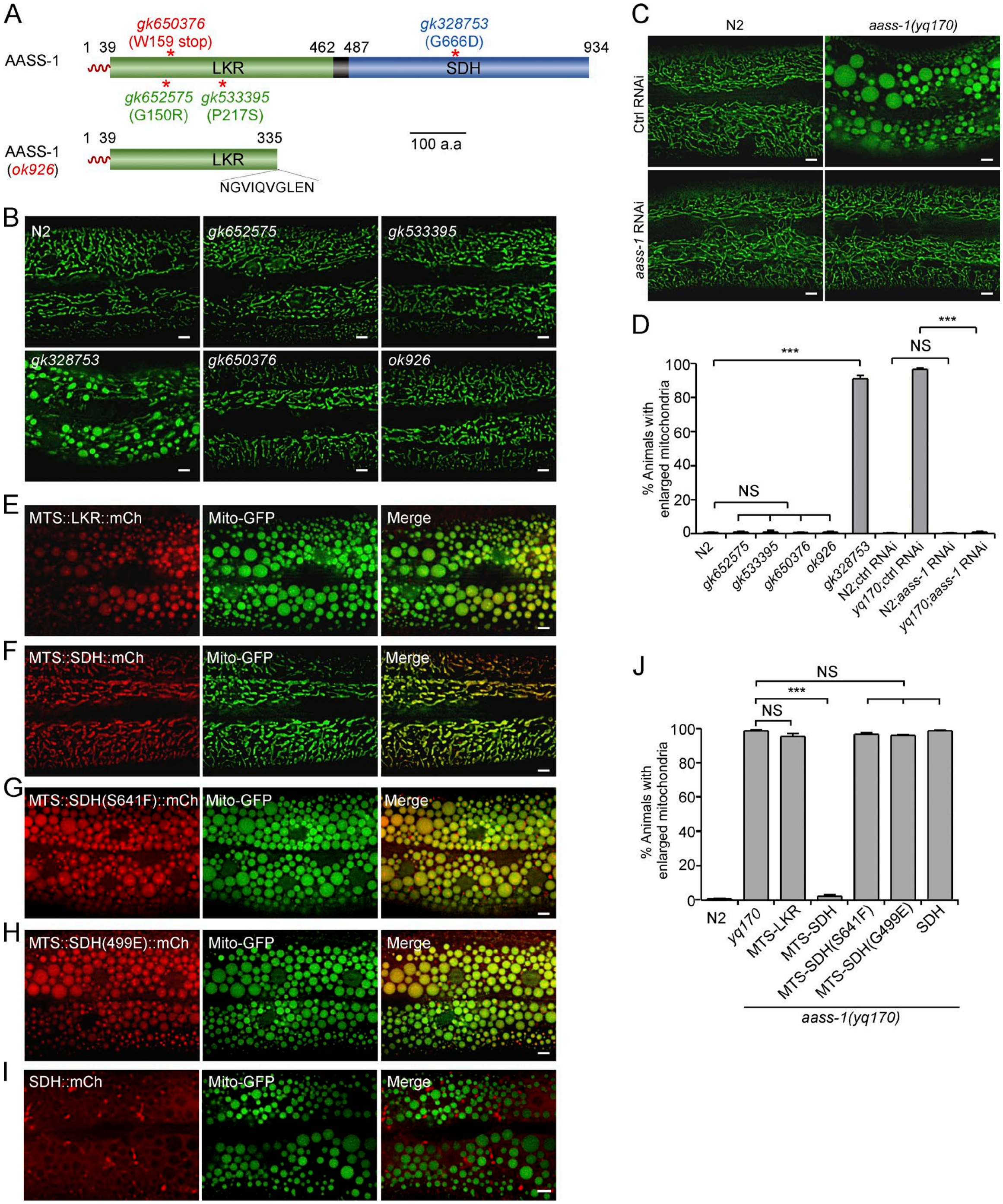

Figure 2. **Mutations in SDH, but not LKR, induce mitochondrial abnormalities. (A)** Schematic representation of full-length AASS-1 and the *ok926* deletion mutant. LKR and SDH are indicated in green and blue, respectively. The wavy line represents the MTS. Point mutations are indicated with asterisks. The 10 frame-shifted amino acids generated by the *ok926* deletion are indicated at the C terminus of the *ok926* deletion mutant. **(B)** Representative images of Mito-GFP–labeled mitochondria in the hypodermis of N2 and *aass-1* mutant animals. Bars, 5 µm. **(C)** Representative images of mitochondria in the hypodermis of control (ctrl) RNAi- and *aass-1* RNAi-treated N2 and *aass-1(yq170)* animals. Bars, 5 µm. **(D)** Quantification of animals with abnormally enlarged mitochondria (area ≥12 µm^2). 90 animals or more were scored for each genotype. **(E–J)** Images (E–I) and quantification (J) of the rescuing effects on *aass-1(yq170)* mitochondria of ectopically expressed MTS- and mCherry-fused LKR (MTS::LKR::mCh; E), SDH (MTS::SDH::mCh; F), SDH(S641F) (MTS::SDH(S641F)::mCh; G), SDH(G499E) (MTS::SDH(G499E)::mCh; H), and nonmitochondrion-targeted SDH::mCh (SDH::mCh; I). Bars, 5 µm. 90 animals or more were scored for each genotype (J). For all quantifications, *, $P < 0.05$; **, $P < 0.01$; and ***, $P < 0.001$. Error bars represent SEM.

mitochondrial damage, did not show defects in ATP production, mitochondrial membrane potential, or adult body lengths (Fig. 3, F–H and J; and Fig. S3, D and E). Thus, mitochondrial damage in the hypodermis impaired adult animal growth.

Mitochondrial dynamics are defective in *aass-1* SDH mutants

To understand how mitochondria were enlarged in *aass-1(yq170)* hypodermis, we performed live-cell imaging to monitor the dynamics of Mito-GFP–labeled mitochondria. In N2 animals,

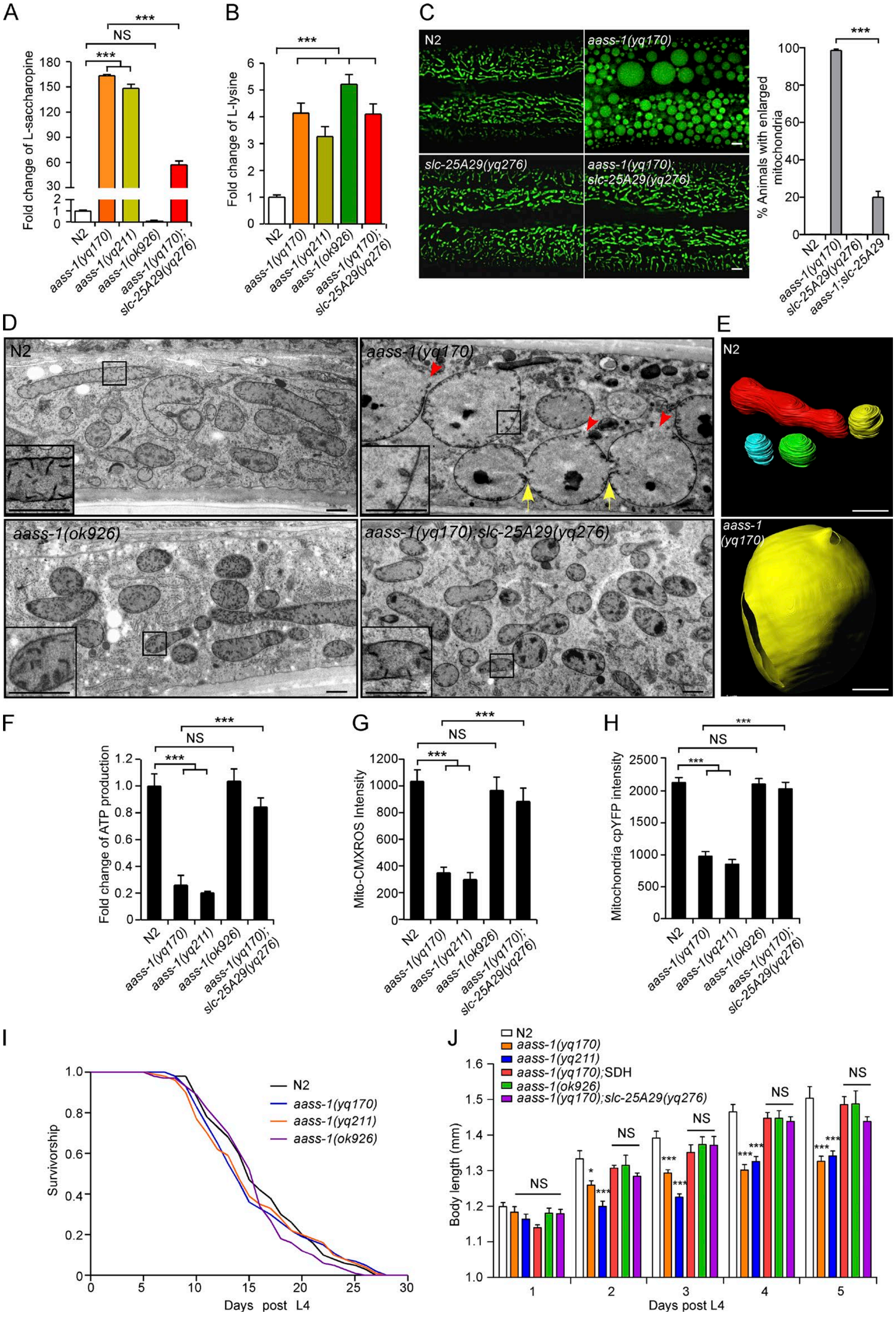

Figure 3. **SDH mutation-induced saccharopine accumulation causes mitochondrial damage and functional loss and shortens *C. elegans* body length. (A and B)** Fold change of saccharopine (A) and lysine (B) levels in animals with the indicated genotypes. Data (mean ± SEM) were derived from three independent experiments as shown in Fig. S2 and normalized to saccharopine or lysine intensities in N2 animals. **(C)** Images (left) and quantification (right) of the suppression of *aass-1(yq170)* mitochondrial defects by *slc-25A29(yq276)* mutation. 90 animals or more were scored for each genotype. Bars, 5 µm. **(D)** TEM images of mitochondria in the hypodermis in adult animals with the indicated genotypes. Boxed regions showing crista structures are magnified (3×) and shown in the bottom left corner in each image. Yellow arrows indicate mitochondrial fusion, and red arrowheads indicate broken mitochondria. Bars, 1 µm. **(E)** Representative images of 3D reconstructed mitochondria in the hypodermis of N2 (top) and *aass-1(yq170)* (bottom) animals. Bars, 1 µm. **(F)** Fold change of ATP levels in the hypodermis of animals with the indicated genotypes. Data (mean ± SEM) are from three independent experiments and normalized to the ATP levels in N2 animals. **(G and H)** Quantification of Mito-CMXROS (G) and Mito-cpYFP (H) intensities in adult animals with the indicated genotypes. 10 synchronized animals were analyzed for each genotype. **(I)** Survival curves of *C. elegans* animals with indicated genotypes. 100 animals were analyzed for each genotype. **(J)** Analysis of body lengths of adult animals with the indicated genotypes. 10 synchronized animals of each genotype were analyzed at every time point. For all quantifications, *, $P < 0.05$; **, $P < 0.01$; and ***, $P < 0.001$. Error bars represent SEM.

mitochondria underwent dynamic fusion and fission, which maintained their predominantly tubular morphology (Fig. 4, A and C; and Video 3). Interestingly, in *aass-1(yq170)* larvae (e.g., L4 stage), we observed that tubular mitochondria underwent retraction and ultimately became spherical, and no tubulation of these spherical mitochondria occurred (Fig. 4 B and Video 4). In *aass-1(yq170)* adult animals, fusions were observed between abnormally enlarged mitochondria, while no fission events were observed during the monitoring period (Fig. 4, B and C; and Video 5). To understand how mitochondrial dynamics was affected in *aass-1* SDH mutants, we examined the mitochondrial recruitment of DRP-1, the *C. elegans* homologue of mammalian DRP1 required for mitochondrial fission (Labrousse et al., 1999). In the WT, GFP-tagged DRP-1, which functionally rescued the over-connected mitochondria in *drp-1(tm1108)* deletion mutants to WT levels (Fig. 4 E), frequently localized to the constriction sites of mitochondria (Fig. 4, F, H, and I). In *aass-1(yq170)* mutants, however, GFP::DRP-1 was found to dock onto spherical mitochondria with much larger diameters than the WT, and no mitochondrial constriction at the docking sites was observed (Fig. 4, G–I). In addition, we found that the ER, labeled with GFP::TRAM-1, crossed mitochondria at the constriction sites in WT but not in *aass-1(yq170)* mutants (Fig. 4 J), which suggests that the ER–mitochondrion interaction was probably affected in the mutants. Altogether, these data suggest that the accumulation of saccharopine in *aass-1* SDH mutants likely impaired DRP-1– and ER-dependent mitochondrial tubulation and fission, while the continuous fusion contributed to the abnormal mitochondrial enlargement. Supporting this conclusion, double mutants of *aass-1(yq170)* with *fzo-1(tm1133)*, a deletion allele of *fzo-1*/MFN1/2 that is required for mitochondrial outer membrane fusion (Breckenridge et al., 2008; Ichishita et al., 2008), exhibited small spherical mitochondria like *fzo-1(tm1133)* single mutants (Fig. 4 D). Similarly, RNAi of *eat-3*/OPA1, which is required for fusion of inner mitochondrial membranes (Kanazawa et al., 2008), suppressed the mitochondrial enlargement in *aass-1(yq170)* animals (Fig. 4 D).

AASS function is evolutionarily conserved between *C. elegans* and mammals

To investigate whether AASS has a conserved function between *C. elegans* and humans, we expressed a *C. elegans* mitochondrion-targeted human AASS tagged with mCherry (MTS::hAASS::mCh) under the control of the hypodermis-specific *Y37A1B.5* promoter. *aass-1(yq170)* animals expressing MTS::hAASS::mCh showed predominantly tubular mitochondrial morphology, indicating that hAASS rescued the mitochondrial defects (Fig. 5, A and C). Similar expression of mitochondrion-targeted human SDH (MTS::hSDH::mCh), but not human LKR (MTS::hLKR::mCh), also rescued the mitochondrial defects in *aass-1(yq170)* animals (Fig. 5, B and C). Expression of hSDH carrying a T719A mutation (MTS::hSDH(T719A)::mCh) found in a human hyperlysinemia patient (Houten et al., 2013) failed to rescue the defective mitochondria in *aass-1(yq170)* mutants (Fig. 5, B and C). These results suggest that the function of AASS is evolutionarily conserved and SDH is required to maintain the morphology and function of mitochondria in humans.

Mutations in LKR or SDH in human AASS (hAASS) lead to two types of hyperlysinemia. Type I hyperlysinemia exhibits an abnormal increase in lysine in the blood and is mostly asymptomatic. Type II hyperlysinemia (saccharopinuria) patients, as reported by a few cases (more than five), have an abnormal increase in both lysine and saccharopine in the blood or urine, and display a variety of developmental disorders to different extent (Carson et al., 1968; Simell et al., 1972; Cederbaum et al., 1979; Cox et al., 1986; Vianey-Liaud et al., 1986; Houten et al., 2013). To investigate whether the mutations found in hAASS in these two types of hyperlysinemia patients can cause abnormal mitochondrial enlargement, we used the CRISPR/Cas9 system to generate point mutations in the *C. elegans aass-1* gene corresponding to hAASS mutations in patients (Fig. S2, E–G). In *aass-1(yq246)* mutant worms, which carried a R71Q mutation corresponding to the R65Q hLKR mutation in a hyperlysinemia patient (Fig. S2, E and F; Houten et al., 2013), the mitochondria exhibited normal morphology (Fig. 5, D and E). In contrast, *aass-1(yq277)* mutants carrying a T729A mutation corresponding to the T719A SDH mutation in a saccharopinuria patient (Fig. S2, E and F) displayed abnormally enlarged mitochondria (Fig. 5, D and E). TEM analysis revealed that *aass-1(yq246)* mitochondria were similar to those in N2 animals, but mitochondria in *aass-1(yq277)* mutants were greatly enlarged and damaged (Fig. 5 F). Both *aass-1(yq246)* and *aass-1(yq277)* mutants had much higher levels of lysine than the WT, but only the *aass-1(yq277)* mutation strongly elevated the saccharopine levels and reduced ATP production (Fig. 5, G–I; and Fig. S1 H). In addition, while *aass-1(yq246)* did not change adult body lengths, *aass-1(yq277)* mutant adults were significantly shorter, like *aass-1(yq170)* mutants (Fig. 5 J). These findings suggest that mutations in human SDH can greatly elevate saccharopine levels and provide further evidence that the accumulation of saccharopine rather than lysine results in abnormal mitochondrial enlargement and damage. Importantly, introducing the *yq246* mutation into *aass-1(yq170)* mutants abrogated the accumulation of saccharopine, while the high level of lysine was unchanged (Fig. 5, G and H; and Fig. S1 H). As a result, *aass-1(yq246yq170)* animals displayed normal mitochondrial morphology, ultrastructure, and ATP production; and their adult body lengths were restored to WT levels (Fig. 5 D–F, I, and J). Thus, inactivating LKR abrogated saccharopine generation and consequently prevented SDH mutation-induced mitochondrial damage and functional loss.

SDH mutation causes saccharopine accumulation and defective development in mice

To investigate whether saccharopine accumulation induces mitochondrial damage in mammals, we generated *Aass* mutant mice carrying the R65Q mutation in LKR or the G489E mutation in SDH (Fig. S4, A and B). *Aass(R65Q)* homozygous mice were viable and developmentally indistinguishable from WT; in contrast, *Aass(G489E)* homozygous mice displayed progressive postnatal growth retardation and succumbed to death at ~6 wk of age (Fig. 6, A–C). *Aass(R65Q)* mice had greatly elevated levels of lysine but not saccharopine in the blood; however, *Aass(G489E)* mice had greatly elevated levels of both lysine and saccharopine (Fig. 6, D and E; and Fig. S4 C). *Aass* expression was mainly detected in the liver (Fig. 6 F), suggesting that the

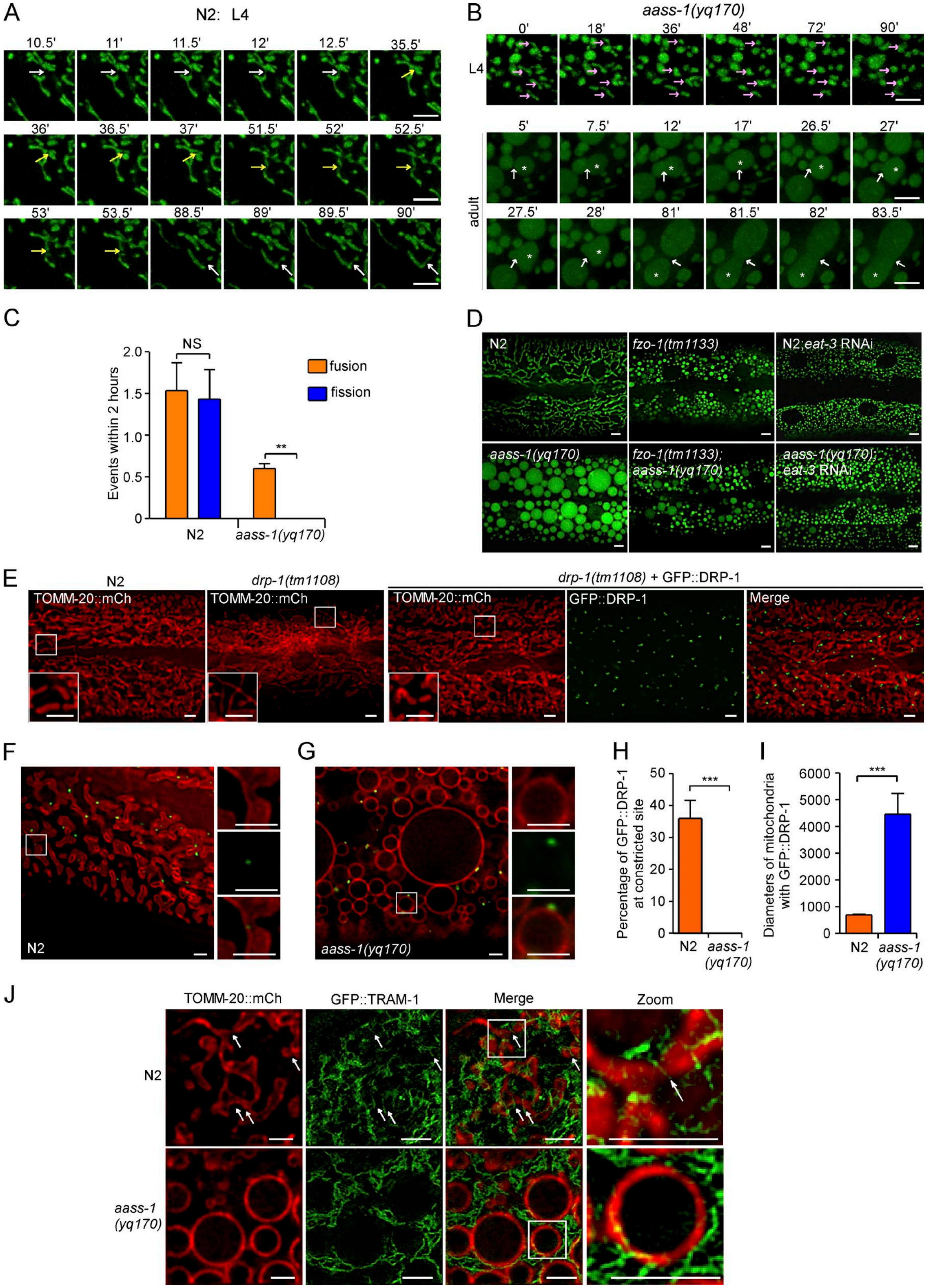

Figure 4. **The dynamics of mitochondria is disrupted in *aass-1* SDH mutants. (A)** Dynamics of Mito-GFP–labeled mitochondria in the hypodermis of an N2 L4 animal. White arrows indicate sites of mitochondrial fusion. Yellow arrows indicate sites of mitochondrial fission. **(B)** Dynamics of Mito-GFP–labeled mitochondria in hypodermal cells in an *aass-1(yq170)* L4 animal and an *aass-1(yq170)* adult animal. White arrows indicate sites of mitochondrial fusion. Purple arrows indicate mitochondria undergoing retraction. Asterisks label mitochondria undergoing fusion in *aass-1(yq170)* animals. Bars, 5 µm. **(C)** Quantification of the frequency of fusion and fission events in N2 and *aass-1(yq170)* mutants. **(D)** Representative images of mitochondria in the hypodermis of N2, *aass-1(yq170)* single mutants, *fzo-1(tm1133)* single mutants, *fzo-1(tm1133);aass-1(yq170)* double mutants, and *eat-3* RNAi-treated N2 and *aass-1(yq170)* animals. Bars, 5 µm.

liver is the major tissue involved in lysine degradation in mice. While *Aass(G489E)* mice had AASS protein levels comparable to the WT in the liver, *Aass(R65Q)* mouse livers did not show detectable AASS protein, similar to that observed in the fibroblast of a human patient (Houten et al., 2013). This suggests that the R65Q mutation affected the protein stability of mammalian AASS (Fig. 6 G). Strikingly, the activities of alanine aminotransferase (ALT) and aspartate aminotransferase (AST) in the blood of *Aass(G489E)* mice were greatly increased by 5–10-fold compared with WT and *Aass(R65Q)* mice (Fig. 6, H and I). In comparison, the activities of creatine kinase (CK), lactate dehydrogenase (LDH), α-hydroxybutyrate dehydrogenase (α-HBDH), and creatine kinase-MB (CKMB), which reflect cardiac functions, showed no significant difference in the blood of WT, *Aass(R65Q)*, and *Aass(G489E)* mice (Fig. S4, F–I). These results indicated that the functions of the liver, but not heart, were severely damaged in *Aass(G489E)* mice. Further examinations revealed that the livers of *Aass(G489E)* mice, but not *Aass(R65Q)* mice, were abnormally enlarged compared with the WT (Fig. 6 J). Like the blood, the livers of *Aass(R65Q)* mice had greatly elevated lysine levels, while the livers of *Aass(G489E)* mice exhibited a strong elevation in both lysine and saccharopine (Fig. 6, K and L; and Fig. S4 D). In addition, the sizes of the hepatocytes in *Aass(G489E)* mice were obviously increased (Fig. S4 E). These results suggest that saccharopine is responsible for the developmental defects and liver abnormalities of *Aass(G489E)* mice.

SDH mutation causes damage of mitochondrial structures and functions in mouse liver

We next examined the ultrastructure of mitochondria in the liver using TEM. The liver mitochondria in *Aass(R65Q)* mice were indistinguishable from those in WT (Fig. 7, A, C, and D). However, the majority of mitochondria in *Aass(G489E)* hepatocytes were greatly enlarged, and the cristae were damaged (Fig. 7, B–D). Moreover, the hepatocyte ATP levels in *Aass(G489E)* mice, but not *Aass(R65Q)* animals, were significantly reduced compared with the WT (Fig. 7 E). To further investigate the mitochondrial defects in the liver, we in vitro cultured hepatocytes isolated from WT and *Aass(G489E)* mice and examined mitochondrial morphologies and dynamics using MitoTracker Green staining (Fig. 7, F and G). In WT hepatocytes, mitochondria exhibited similar tubular morphologies, and underwent dynamic fusion and fission (Fig. 7 F and Video 6). However, mitochondria in *Aass(G489E)* hepatocytes were abnormally enlarged, and no obvious dynamics were observed over the whole monitoring period (Fig. 7 G and Video 7). We next examined the levels of oxygen consumption. Whereas *Aass(R65Q)* and WT mitochondria had similar levels of oxygen consumption rate (OCR), *Aass(G489E)* mitochondria had much lower oxygen consumption than the WT (Fig. 7, H and I). Taken together, these findings suggest that, like in *C. elegans*, mutation of SDH in AASS blocked saccharopine metabolism, which caused damage and functional loss of mitochondria in hepatocytes.

Inactivation of genes required for mitochondrial α-ketoglutarate production suppresses SDH mutation–induced saccharopine accumulation and mitochondrial defects

We finally sought to identify additional factors that, when inactivated, could rescue the mitochondrial defects caused by SDH mutation-induced saccharopine accumulation. By performing an *aass-1(yq170)* suppressor screen, we obtained two mutants, *yq274* and *yq275*. Both mutants strongly suppressed the abnormal mitochondrial enlargement and damage in *aass-1(yq170)* hypodermis (Fig. 8, A–C). *yq274* and *yq275* greatly reduced the levels of saccharopine in *aass-1(yq170)* mutants (Figs. 8 D and S1 H). Intriguingly, the lysine levels were also decreased in double mutants of *aass-1(yq170)* with *yq274* or *yq275* compared with *aass-1* single mutants (Figs. 8 E and S1 H). The *yq274* and *yq275* mutations also restored the defective ATP production and ameliorated the shortened adult body lengths of *aass-1(yq170)* animals (Fig. 8, G and H). Using single nucleotide polymorphism (SNP)–based mapping and sequencing, we identified that *yq274* caused a D185N mutation in the *slc-25A18.1* gene, which encodes an orthologue of the human mitochondrial glutamate carriers SLC25A18 and SLC25A22; and *yq275* caused a G8D mutation in the *gdh-1* gene, which encodes an orthologue of human glutamate dehydrogenase (GDH), the enzyme responsible for converting glutamate into α-ketoglutarate and ammonia (Fig. S5, A and B; Hudson and Daniel, 1993; Fiermonte et al., 2002). Indeed, α-ketoglutarate levels in double mutants of *aass-1(yq170)* with *yq274* or *yq275* were reduced compared with N2 and *aass-1(yq170)* worms (Fig. 8 F). Expression of mCherry-tagged SLC-25A18.1 and GDH-1 indicated that they localized to mitochondria and rescued the abnormal mitochondrial morphologies in double mutants of *aass-1(yq170)* with *yq274* or *yq275* so that they resembled *aass-1(yq170)* single mutants (Fig. S5, C–E). Together these data suggest that inactivation of SLC-25A18.1 or GDH-1 probably reduces saccharopine generation by inhibiting mitochondrial α-ketoglutarate generation (Fig. 8, F and I) and restores mitochondrial structures and functions. Supporting this notion, the *ok3184* deletion of *idh-2*, which encodes an isocitrate dehydrogenase (IDH) that converts isocitrate to α-ketoglutarate, also strongly suppressed the mitochondrial defects in *aass-1(yq170)* mutants (Fig. 8, A–C). Compared with *aass-1(yq170)* single mutants, *aass-1;idh-2* double mutants had reduced levels of lysine, α-ketoglutarate, and saccharopine, and the ATP production and

---

(E) Images of the rescuing effects on *drp-1(tm1108)* mitochondria of GFP::DRP-1. Bars, 5 µm. Boxed regions of mitochondria are magnified (3×) and shown in the bottom left corners of the corresponding images. **(F and G)** Representative images of TOMM-20::mCherry-labeled mitochondria and GFP::DRP-1 in the hypodermis of N2 (F) and *aass-1(yq170)* (G) animals. Boxed regions are magnified (3×) and shown on the right of each image. Bars, 3 µm. **(H)** Percentage of GFP::DRP-1 at mitochondrial constriction sites in N2 and *aass-1(yq170)* animals. Five animals were analyzed for each genotype. **(I)** Diameters of mitochondria positive for GFP::DRP-1 in N2 and *aass-1(yq170)* animals. Five animals were analyzed for each genotype. **(J)** Representative images of TOMM-20::mCh-labeled mitochondria and GFP::TRAM-labeled ER in the hypodermis of N2 and *aass-1(yq170)* animals. Boxed regions are magnified (3×) and shown on the right of each image. Arrows indicate the sites where mitochondria are crossed by ER tubules. Bars, 5 µm. For all quantifications, *, $P < 0.05$; **, $P < 0.01$; and ***, $P < 0.001$. Error bars represent SEM.

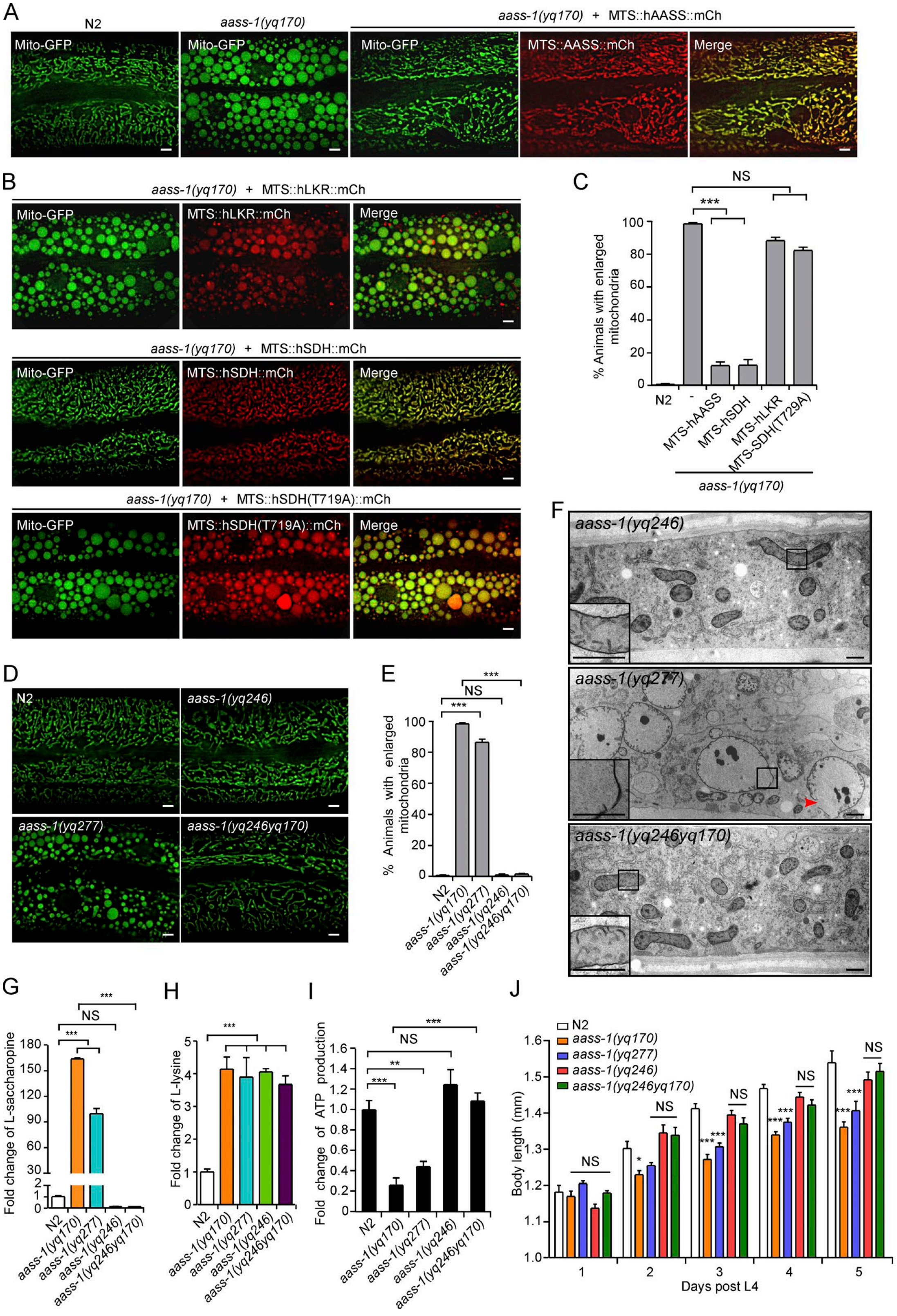

Figure 5. **AASS functions are evolutionarily conserved between *C. elegans* and humans. (A)** Images representing the rescuing effect on *aass-1(yq170)* mitochondria by ectopic expression of worm MTS- and mCherry-fused hAASS (MTS::hAASS::mCh). Bars, 5 µm. **(B)** Images representing the rescuing effects on *aass-1(yq170)* mitochondria by ectopic expression of worm MTS- and mCherry-fused hLKR (MTS::hLKR::mCh; top), hSDH (MTS::hSDH::mCh; middle), and hSDH(T719A) (MTS::hSDH(T719A)::mCh; bottom). Bars, 5 µm. **(C)** Quantification of animals as shown in A and B with abnormally enlarged mitochondria (area ≥12 µm^2). 90 animals or more were scored for each genotype. **(D and E)** Images (D) and quantification (E) of enlarged mitochondria in N2 animals and *aass-1* mutants (*yq246*, *yq277*, and *yq246yq170*) containing mutations corresponding to hAASS mutations in hyperlysinemia patients. 90 animals or more were scored for each genotype. Bars, 5 µm. **(F)** TEM images of mitochondria in hypodermal cells in *aass-1(yq246)*, *aass-1(yq277)*, and *aass-1(yq246yq170)* animals. Boxed

body lengths were mostly restored (Fig. 8, D–I; and Fig. S1 F). Taken together, these findings suggest that inhibition of the key factors required for mitochondrial α-ketoglutarate production ameliorates the mitochondrial damage caused by saccharopine accumulation resulting from SDH mutations.

Discussion

Our findings demonstrated that mitochondrial degradation of the lysine catabolism intermediate saccharopine is required for maintenance of normal mitochondrial dynamics and functions. In *C. elegans*, SDH mutations of AASS-1 caused a marked accumulation of saccharopine, which in turn disrupted mitochondrial dynamics, leading to mitochondrial damage and functional loss (Fig. 8 I). *C. elegans* animals accumulating saccharopine-induced mitochondria in the hypodermis exhibited reduced adult growth but not life span. In mice, failed saccharopine metabolism resulting from SDH mutation similarly causes mitochondrial damage and functional impairment in the liver, leading to liver hypertrophy. Altogether, these defects lead to postnatal growth retardation and death of *Aass* SDH mutant mice. In both *C. elegans* and mice, however, mitochondria seem to tolerate the high levels of lysine resulting from LKR mutations. Thus, abnormally accumulated saccharopine rather than lysine in the lysine degradation pathway is toxic to mitochondria.

Our results demonstrate that AASS function is evolutionarily conserved between *C. elegans* and mammals. Expression of full-length human AASS and SDH, but not LKR, fully rescued the mitochondrial defects in *C. elegans* SDH mutants. Moreover, *C. elegans* mutants carrying the mutation corresponding to a SDH mutation identified in a hyperlysinemia patient displayed strongly elevated saccharopine levels, abnormally enlarged and damaged mitochondria, and reduced ATP levels. These results, together with the findings in SDH mutant mice, suggest that hyperlysinemia II (saccharopinuria) is in fact a genetic mitochondrial disorder. This provides a mechanistic basis to distinguish between the asymptomatic hyperlysinemia I and the detrimental saccharopinuria. Using unbiased genetic suppressor screens, we identified essential factors and metabolic pathways that, when inactivated, rescued the mitochondrial defects caused by SDH mutation–induced saccharopine accumulation in *C. elegans* (Fig. 8 I). These factors include the mitochondrial glutamate importer SLC-25A18.1, the mitochondrial GDH GDH-1, and the mitochondrial IDH IDH-2, all of which are involved in mitochondrial α-ketoglutarate production. Based on our findings, potential therapeutic strategies can be designed for treatment of saccharopinuria. For example, small-molecule compounds can be developed to inhibit the activities of LKR, the mitochondrial lysine importer, and the essential factors required for mitochondrial α-ketoglutarate production. In this way, the SDH mutation–induced accumulation of mitochondrially toxic saccharopine and the resulting mitochondrial damage can probably be ameliorated.

Because amino acid catabolism usually occurs in mitochondria, our findings suggest that aberrant amino acid catabolism can result in mitochondrial defects and consequently functional loss. This provides mechanistic insights for understanding mitochondrial homeostasis under metabolic stresses and suggests that, for aminoacidopathies of unknown etiology, the pathogenesis could result from perturbed mitochondrial homeostasis.

Materials and methods

C. elegans strains and genetics

C. elegans cultures and genetic crosses were performed following standard procedures. The Bristol N2 strain was used as WT. *aass-1(yq170)*, *aass-1(yq211)*, *aass-1(yq170);slc-25A18.1(yq274)*, and *aass-1(yq170);gdh-1(yq275)* mutants were obtained by EMS mutagenesis. *aass-1(yq246)*, *aass-1(yq277)*, *aass-1(yq246yq170)*, and *slc-25A29(yq276)* were generated with the CRISPR/Cas9 system. The *fzo-1(tm1133)* deletion mutant was provided by S. Mitani, Tokyo Women's Medical University, Tokyo, Japan. The following mutants used in this study were provided by the *Caenorhabditis* Genetics Center (University of Minnesota, Minneapolis, MN): LGIV: *aass-1(gk652575)*, *aass-1(gk650376)*, *aass-1(gk533395)*, *aass-1(gk328753)*, *aass-1(ok926)*; LGV: *unc-76(e911)*. LGX: *idh-2(ok3184)*. The integrated arrays *qxIs615* ($\mathrm{P}_{y37a1b.5}$*luciferase::gfp*) and *qxIs258* ($\mathrm{P}_{ced\text{-}1}$*nuc-1::mCherry*) and the extrachromosomal array *qxEx3928* ($\mathrm{P}_{y37a1b.5}$*MANS::gfp*) were provided by X. Wang, Institute of Biophysics, Chinese Academy of Sciences, Beijing, China. The integrated arrays *hqIs181* ($\mathrm{P}_{sdhl\text{-}1}$*mtLs::gfp*) and *opIs334* ($\mathrm{P}_{ced\text{-}1}$*yfp::2×FYVE*) were provided by M. Dong, National Institute of Biological Sciences, Beijing, China, and M.O. Hengartner, University of Zurich, Zurich, Switzerland. The integrated arrays *yqIs25* ($\mathrm{P}_{lgg\text{-}1}$*gfp::lgg-1*), *yqIs157* ($\mathrm{P}_{y37a1b.5}$*mito-gfp*), *yqIs179* ($\mathrm{P}_{y37a1b.5}$*tomm-20::mCherry*), *yqIs189* ($\mathrm{P}_{col\text{-}19}$*mito-cpYFP*), and *yqIs199* ($\mathrm{P}_{vha\text{-}6}$*luciferase::gfp*) were generated in this laboratory. Integrated arrays, deletion strains, and mutants generated by EMS mutagenesis or CRISPR/Cas9 were outcrossed with the N2 strain at least four times.

Expression vectors

Expression vectors used for generating transgenic strains were constructed using standard protocols and are listed in Table S1.

EMS screen and gene cloning

To screen for mutants with abnormal mitochondrial morphology, synchronized L4-stage *yqIs157* animals were treated with 50 mM EMS for 4 h. The F2 progeny of EMS-treated animals were grown to the age of 24–48 h after the L4 molt at 20°C and observed under fluorescent microscopes. From a screen of 12,000 haploid

regions showing crista structures are magnified (3×) and shown in the bottom left corner in each image. The red arrowhead indicates a broken mitochondrial membrane. Bars, 1 µm. **(G and H)** Fold change of saccharopine (G) or lysine (H) levels in N2, *aass-1(yq170)*, *aass-1(yq246)*, *aass-1(yq277)*, and *aass-1(yq246yq170)* animals. Data (mean ± SEM) are from three independent experiments as shown in Fig. S2 and are normalized to the levels of saccharopine or lysine in N2 animals. **(I)** Fold change of ATP levels in the hypodermis of the indicated animals. Data (mean ± SEM) are from three independent experiments and are normalized to ATP levels in N2 animals. **(J)** Analysis of body lengths of adult animals with the indicated genotypes. 10 synchronized animals of each genotype were analyzed at every time point. Comparisons are between N2 and mutants. For all quantifications, *, $P < 0.05$; **, $P < 0.01$; and ***, $P < 0.001$. Error bars represent SEM.

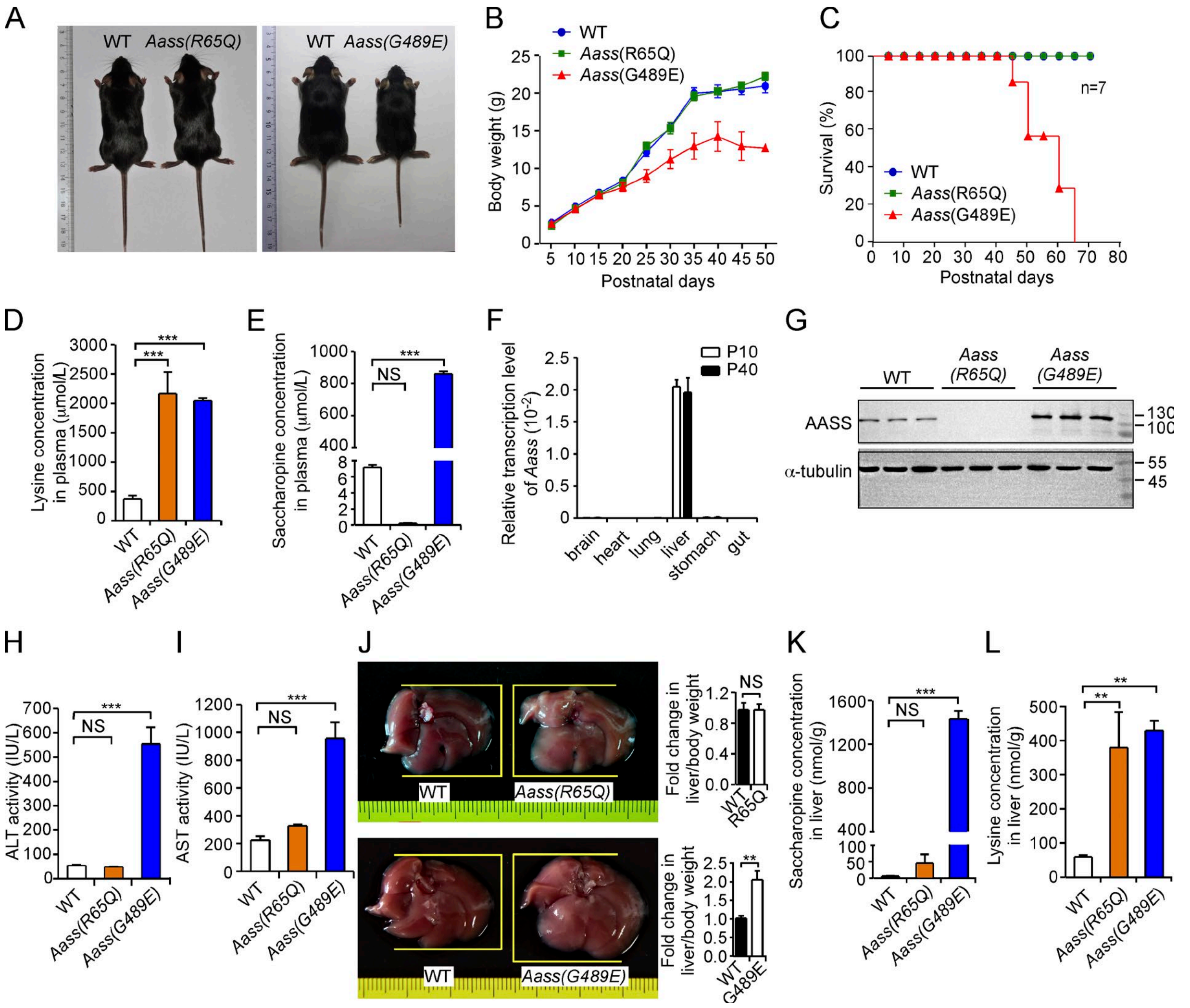

Figure 6. **Saccharopine accumulation leads to mouse liver hypertrophy and defective postnatal growth. (A)** Representative images of WT, *Aass(R65Q)*, and *Aass(G489E)* mice at P40. **(B)** Growth curves of WT, *Aass(R65Q)*, and *Aass(G489E)* knock-in mice. *n* = 7. **(C)** Survival curves of postnatal WT, *Aass(R65Q)*, and *Aass(G489E)* mice. *n* = 7. **(D and E)** Plasma lysine (D) and saccharopine (E) levels in WT, *Aass(R65Q)*, and *Aass(G489E)* mice. Data (mean ± SEM) are from four mice (as measured in Fig. S4 C) and are normalized to the WT value. **(F)** Quantitative real-time PCR analysis of *Aass* expression in different mouse tissues. Data (mean ± SEM) are from four independent experiments and are normalized to the *Gapdh* value. **(G)** Western blot of AASS protein in the livers of WT, *Aass(R65Q)*, and *Aass(G489E)* mice. α-Tubulin was used as the internal control. Three animals were analyzed for each genotype. **(H and I)** Plasma ALT (H) and AST (I) activities of WT, *Aass(R65Q)*, and *Aass(G489E)* mice. Data (mean ± SEM) are from four or more mice at P40. **(J)** Images (left) and ratio of liver to body weight of WT and *Aass(R65Q)* (top) and of WT and *Aass(G489E)* (bottom) mice at P40. *n* = 4. **(K and L)** Lysine (K) and saccharopine (L) levels in the livers of WT, *Aass(R65Q)*, and *Aass(G489E)* mice. Data (mean ± SEM) are from four mice (as measured in Fig. S4 D). Error bars represent SEM.

genomes, we isolated 24 mutants that displayed morphologically abnormal mitochondria. Among these mutants, *yq170* and *yq211* contained similarly enlarged and spherical mitochondria. Complementation tests suggested that they affected the same gene. *yq170* was mapped to the left of genetic map position −26.01 [Snp-Y66H1A(17273)] on LG IV using SNP mapping (Davis et al., 2005). Genomic sequencing revealed that *yq170* contains a C-to-T mutation in the *R02D3.1* gene, which results in substitution of Ser 641 with Phe, and *yq211* contains a G-to-A transition, which causes substitution of Gly 499 with Glu.

To screen for mutations that suppress the mitochondrial abnormality in *aass-1(yq170)* mutants, L4-stage *aass-1(yq170)* animals were mutated with EMS, and the F2 progeny were observed as described above. Two mutants, *yq274* and *yq275*, were isolated from a screen of 3,000 haploid genomes. *yq274* was mapped to the right arm of LG X between genetic map positions 19.12 [Snp-C26G2(29365)] and 22.23 [Snp-F59D12(15190)] by SNP mapping. *yq275* was mapped to the right arm of LG IV between genetic map positions 3.76 [Snp-D2096(39721)] and 6.83 [Snp-K10D11(1231)]. Genomic sequencing revealed that *yq274* contains a G-to-A mutation in the *slc-25A18.1* gene, resulting in substitution of Asp 185 with Asn, and *yq275* contains a G-to-A transition in the *gdh-1* gene, causing substitution of Gly 8 with Asp.

RNAi

C. elegans RNAi experiments were performed by bacterial feeding as described previously (Chen et al., 2010). Briefly, L4 animals were placed on plates seeded with bacteria expressing either

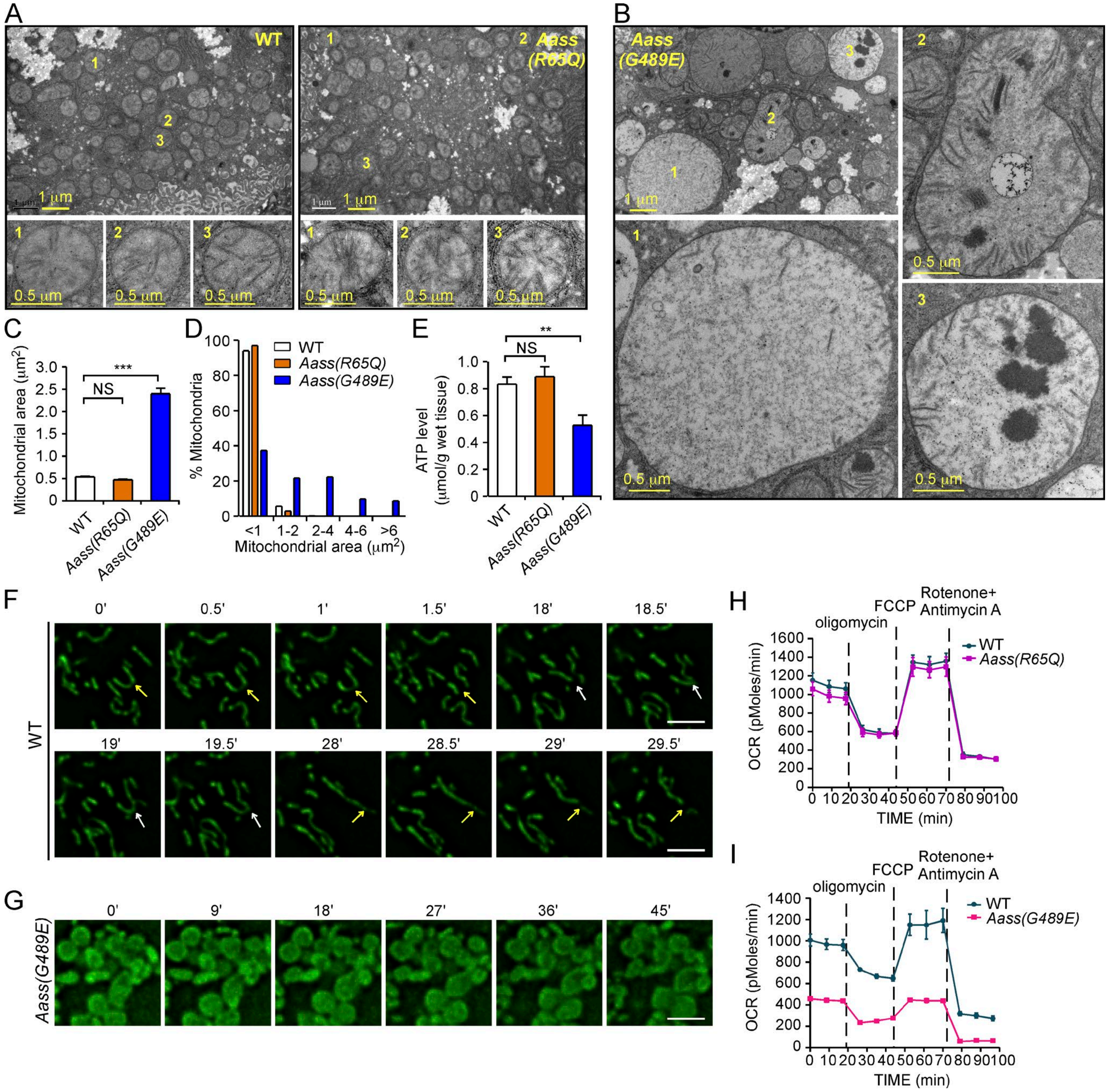

Figure 7. **Saccharopine accumulation induces mitochondrial damage and functional loss in mouse livers. (A and B)** TEM images of mitochondria in the livers of WT, *Aass(R65Q)* (A), and *Aass(G489E)* (B) mice. Representative mitochondria indicated with numbers are magnified (3×) below each image (WT and *Aass(R65Q)*) or shown to the right and below (*Aass(G489E)*). **(C and D)** The average sizes (C) of mitochondria and the percentage of mitochondria with different sizes (D) in the livers of the indicated mice. ≥400 mitochondria were analyzed for each genotype. **(E)** ATP levels in the livers of WT, *Aass(R65Q)*, and *Aass(G489E)* mice. Data (mean ± SEM) are from five mice. **(F and G)** Dynamics of MitoTracker Green–labeled mitochondria-cultured hepatocytes in WT (F) and *Aass(G489E)* (G) mice. White and yellow arrows indicate sites of mitochondrial fusion and fission, respectively. Bars, 5 µm. **(H and I)** OCR in hepatocytes of WT and *Aass(R65Q)* mice (H) and WT and *Aass(G489E)* mice (I) under basal conditions and in response to the indicated mitochondrial inhibitors. Data are from four independent experiments. For all quantifications, *, $P < 0.05$; **, $P < 0.01$; and ***, $P < 0.001$. Error bars represent SEM.

control double-strand RNA or gene-specific double-strand RNA and cultured at 20°C. F1 progeny were observed under fluorescent microscopes when they grew to the age of 48 h after the L4 molt.

Generation of *C. elegans* mutants using CRISPR/Cas9

single-guide RNA (sgRNA) targeting sequences were designed using the online CRISPR design tool and cloned into the pPD162 vector (Dickinson et al., 2013) to generate sgRNA-expressing vectors. Repair templates containing the mutations of interest and additional silent mutations were designed to remove the cleavage sites and introduce restriction sites. *dpy-10* was used as a conversion marker (Arribere et al., 2014). The sgRNA vector (20 ng/µl) and repair template (2 µM) for the target gene were coinjected with the sgRNA construct (15 ng/µl) and repair template

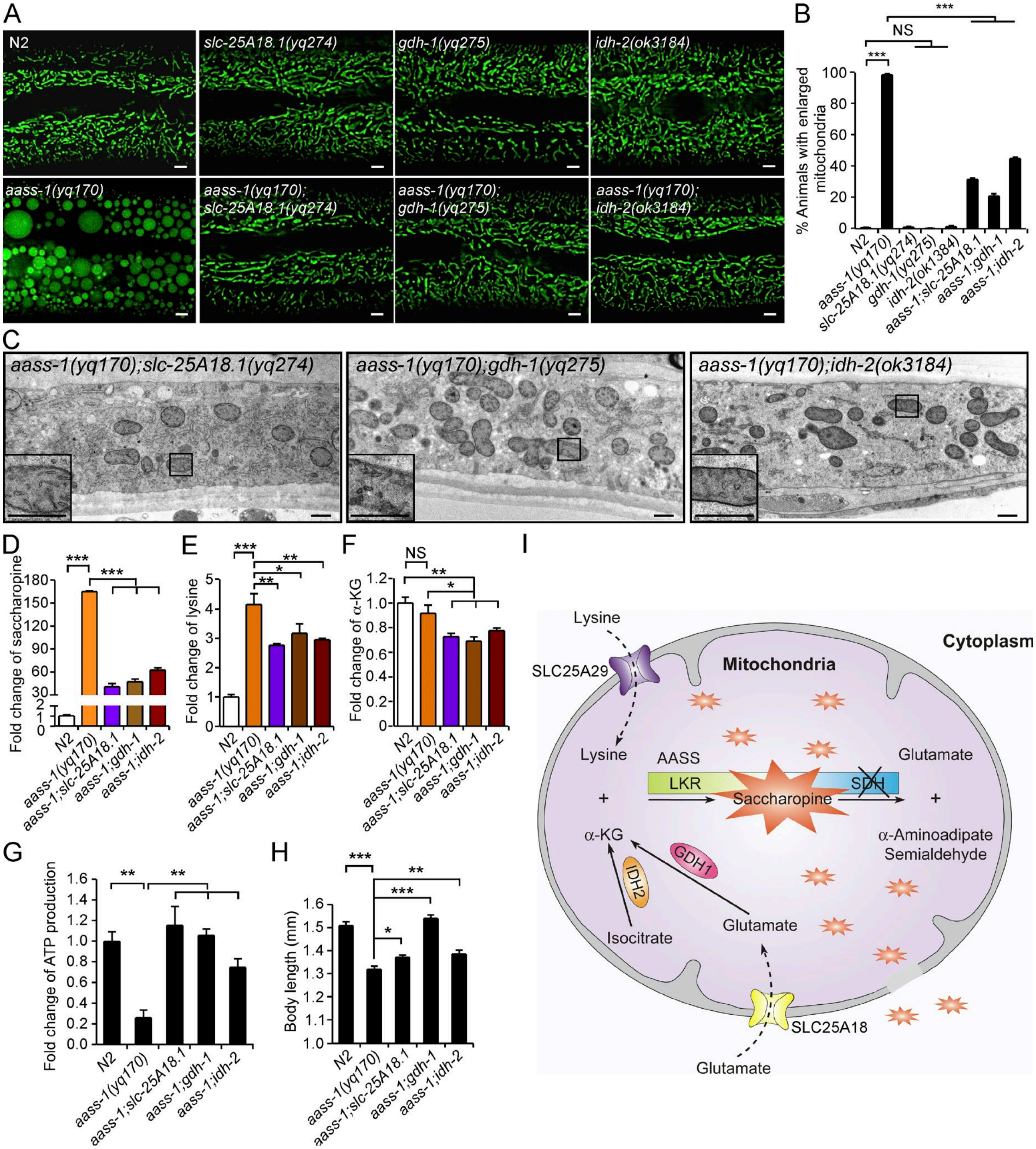

Figure 8. **Inactivation of genes required for mitochondrial β-ketoglutarate generation suppresses saccharopine accumulation and mitochondrial defects in *aass-1(yq170)* mutants. (A and B)** Images (A) and quantification (B) of mitochondria in the hypodermis of N2, *aass-1(yq170)*, *slc-25A18.1(yq274)*, *gdh-1(yq275)*, *idh-2(ok3184)*, *aass-1(yq170);slc-25A18.1(yq274)*, *aass-1(yq170);gdh-1(yq275)*, and *aass-1(yq170);idh-2(ok3184)* animals. 90 animals or more were scored for each genotype. Bars, 5 µm. **(C)** TEM images of mitochondria in hypodermal cells in *aass-1(yq170);slc-25A18.1(yq274)*, *aass-1(yq170);gdh-1(yq275)*, and *aass-1(yq170);idh-2(ok3184)* double mutants. Boxed regions showing crista structures are magnified (3×) and shown in the bottom left corner in each image. Bars, 1 µm. **(D and E)** Relative levels of saccharopine (D) and lysine (E) in N2, *aass-1(yq170), aass-1(yq170);slc-25A18.1(yq274), aass-1(yq170);gdh-1(yq275)*, and *aass-1(yq170);idh-2(ok3184)* animals. Data (mean ± SEM) are from three independent experiments as shown in Fig. S2 and are normalized to saccharopine or lysine levels in N2 animals. **(F)** Relative levels of α-ketoglutarate (α-KG) in N2, *aass-1(yq170), aass-1(yq170);slc-25A18.1(yq274), aass-1(yq170);gdh-1(yq275)*, and *aass-1(yq170);idh-2(ok3184)* animals. Data (mean ± SEM) are from three independent experiments and are normalized to α-ketoglutarate levels in N2 animals. **(G)** Relative ATP levels in the hypodermis of animals with the indicated genotypes. Data (mean ± SEM) are from three independent experiments and are normalized to the ATP level in N2 animals. **(H)** Analysis of body lengths of adult animals (day 5 of adulthood) with the indicated genotypes. 10 synchronized animals were analyzed for each genotype. **(I)** Graphic summary of the metabolic pathways involved in lysine catabolism and of the mitochondrial damage induced by saccharopine accumulation. For all quantifications, *, $P < 0.05$; **, $P < 0.01$; and ***, $P < 0.001$. Error bars represent SEM.

(1 µM) for *dpy-10* into gonads of young adult animals. Rolling F1 progeny (+/*dpy-10*) were singled to produce F2 progeny, which were screened by PCR amplification and restriction digestion. Single progeny of F1 mutants were further isolated on individual plates and analyzed for homozygous mutations. All mutations were confirmed by sequencing. sgRNA targeting sequences and the corresponding 3′ PAM sequences for the relevant genes are listed in Table S2.

MitoTracker Red CMXRos staining

Aged *C. elegans* animals (2 d after L4 molt) were soaked in 50 µl MitoTracker Red CMXRos (2.5 µM in M9 buffer; Invitrogen) for 10 min at 20°C in the dark. Worms were then transferred to a bacterium OP50-seeded NGM plate and allowed to recover for 2 h at 20°C in the dark and examined by fluorescent microscopy.

Microscopy and imaging analysis

Larvae or adult worms were mounted on 3% agar pads in M9 buffer with 2.5 mM levamisole. Differential interference contrast (DIC), GFP, and Mito-GFP in the intestine and body wall muscles were captured with an inverted FV1000 confocal microscope system (IX81; Olympus) using a 60× 1.42-NA oil objective. Other fluorescence images were obtained under a 100× 1.40-NA oil objective using the DeltaVision imaging system (DV Elite; GE Healthcare), with a *Z*-series of 0.3 µm/section for three sections. Images were deconvoluted with the Enhanced Ratio option then cropped with the Boarder Rolloff option, and the *Z*-series of the mitochondria were projected to form one image using the maximum-intensity projection option in softWoRx software coupled with DV Elite. The free Java image-processing program ImageJ was used for measurement of fluorescence intensity and mitochondrial size.

Time-lapse imaging

L4 or adult animal worms (≤7) were anesthetized in 2 µl M9 buffer with 2.5 mM levamisole and covered by a 3% agar pad in a glass-bottom dish (MatTek). Fluorescent images were captured at 20°C under a 100× 1.40-NA oil objective using the DeltaVision imaging system. A piece of tissue paper saturated with water was used to maintain the humidity in the dish. Viability of animals was examined by rescuing them to a NGM plate after imaging. For monitoring mitochondrial dynamics, images were captured every 30 s for 120 min, with a *Z*-series of 0.3 µm/section for a total of 20 sections for each time point. Images were deconvoluted, cropped, and projected as described above.

For monitoring mitochondrial dynamics in cultured mouse hepatocytes, images were captured every 30 s for 60 min, with a *Z*-series of 0.3 µm/section for a total of three sections for each time point. Fluorescent images were captured at 37°C under a 100× 1.40-NA oil objective using the DeltaVision imaging system. Images were deconvoluted, cropped, and projected as described above.

ATP measurements

100 adult worms (day 2 of adulthood) were first picked to a well containing 50 µl M9, and then 50 µl luminescence buffer (0.15 mM D-luciferin, 1% DMSO, and 0.05% Triton X-100, all final concentrations) was added to each well. After incubation for 3 min, luminescence was measured in a Clarity microplate luminometer (Biotek) in the visible spectral range between 300 and 600 nm.

To measure the ATP level in mouse liver, 100 mg liver tissue was homogenized in 500 µl lysis buffer (ATP-Lite Assay kit; Vigorous) using an Ultra-Turrax (IKA). The mixture was ultrasonicated for 2 min using an Ultrasonic Homogenizer 4710 (Cole-Parmer) and boiled for 5 min, and then centrifuged at 10,000 *g* for 5 min at 4°C. 10 µl supernatant was used for luciferin-luciferase assays.

Body length measurements

To measure the body lengths of adult animals, L4 animals were picked to fresh plates and cultured at 20°C for 1 d, 2 d, 3 d, 4 d, or 5 d. Worms were mounted on 3% agar pads in M9 buffer containing 2.5 mM levamisole and photographed under an Axioimager M1 (100× 1.3-NA oil objective; Carl Zeiss) coupled with an AxioCam monochrome digital camera and Axiovision release 4.7 software. All length measurements were performed with ImageJ. Animals were measured from the nose to the tail tip.

Life span assays

100 L4 worms were cultured on fresh plates and transferred to new plates every 2 d until the reproduction ceased. Worms were examined for viability every day. Animals were scored as dead if they had no response to taps on the head and tail.

Saccharopine and lysine measurement

Worms cultured on NGM plates were collected and lyophilized. About 30 mg dry weight worms were extracted with 1.5 ml of 70% aqueous ethanol (vol/vol). 3,4-dihydroxyphenylalanine (DOPA; 2.5 µM) was used as the internal standard. After shaking for 20 min and ultrasonic extraction for another 20 min, the extract was centrifuged at 12,000 rpm for 10 min at 4°C. 1 ml supernatant was transferred to a fresh tube and lyophilized. The lyophilized residue was redissolved in 0.2 ml 20% acetonitrile (vol/vol). After centrifuging at 12,000 rpm for 10 min at 4°C, 0.02 ml supernatant was diluted 10 times with 70% aqueous ethanol (vol/vol) containing DOPA (2.5 µM). The diluted extract was derivatized with a Waters AccQ-Tag derivation kit for analysis of lysine and saccharopine using a protocol described previously (Zhang et al., 2013). The derivatives were analyzed with a UPLC-MS/MS system consisting of an Agilent 1290 Infinity LC pump and a 6495 triple quadruple mass spectrometer (Agilent).

To measure lysine and saccharopine levels in mouse plasma, 20 µl of mouse plasma was extracted with 30 µl of 70% aqueous ethanol (vol/vol). DOPA (2.5 µM) was used as an internal standard. After shaking for 1 min, the extract was centrifuged at 12,000 rpm for 10 min at 4°C. 10 µl supernatant was derivatized and analyzed as above.

To measure lysine and saccharopine levels in mouse livers, 50 mg of liver tissue was collected, snap-frozen in liquid nitrogen, homogenized, and ultrasonicated in 500 µl ddH$_2$O. The homogenates were then lyophilized and extracted with 1.5 ml of 70% aqueous ethanol (vol/vol). DOPA (2.5 µM) was used as an internal standard. After shaking for 1 min, the extract was centrifuged at

12,000 rpm for 10 min at 4°C. 20 µl supernatant was derivatized and analyzed as above.

α-Ketoglutarate measurement

300 adult worms (day 2 of adulthood) cultured on NGM plates were collected in 500 µl ddH_2O and ultrasonicated for 2 min using an Ultrasonic Homogenizer 4710 (Cole-Parmer). The homogenates were then centrifuged at 10,000 *g* for 5 min at 4°C. 10 µl supernatant was used for α-ketoglutarate mesurement by using the α-ketoglutarate Assay Kit (ab83431; Abcam) following the supplier's instructions.

TEM analysis

To examine mitochondrial ultrastructure in *C. elegans*, adult animals (day 2 of adulthood) were rapidly frozen using a high-pressure freezer (EM-ICE; Leica Biosystems). Freeze substitution was performed in anhydrous acetone containing 1% osmium tetroxide. The samples were incubated sequentially at −90°C for 72 h, −60°C for 8 h, and −30°C for 8 h and were finally brought to 0°C for 6 h in a freeze-substitution unit (EM AFS2; Leica Biosystems). The samples were washed and electron-stained with 0.01% uranyl acetate in anhydrous acetone and then gradually infiltrated with Embed-812 resin in the following steps: resin/acetone 1:3 for 3 h, 1:1 for 5 h, 3:1 overnight, and 100% resin three times for 4 h each. Samples were then embedded at 60°C for 48 h. The fixed samples were cut into 70-nm sections with a microtome EM UC7 (Leica Biosystems) and electron-stained with uranyl acetate and lead citrate. Sections were observed with a JEM-1400 (JEOL) operating at 80 kV. To examine mitochondrial ultrastructure in mice, mice were perfused with 2.5% glutaraldehyde and 1% PFA in 0.1 M phosphate buffer (pH 7.2). Then the livers were isolated, cut, and fixed overnight at 4°C with 0.1 M phosphate buffer containing 2.5% glutaraldehyde. Fixed samples were rinsed with PBS and further fixed with 1% OsO_4 for 2 h at 4°C. The samples were rinsed with distilled water and electron-stained with 2% uranyl acetate, then dehydrated by sequential incubation in an acetone series (30%, 50%, 70%, 80%, 90%, 95%, 100%, and 100%, 10 min each). Samples were infiltrated, embedded, cut, stained, and observed as described above.

Electron 3D reconstruction

The ultrastructural 3D study was performed with a Helios Nanolab 600i dual-beam scanning electron microscope (FEI), which combines high-resolution field-emission scanning electron microscope with a focused beam of gallium ions. Adult worms (day 2 of adulthood) were treated with high-pressure freezing, freeze-substitution, and embedding as described above. Then sequential automated focused ion beam milling and scanning electron microscope imaging were performed. To reconstruct the mitochondria, the block face was photographed with a total image size of 2,048 × 1,768 pixels and a field size of 13.8 × 11.9 µm. An acceleration voltage of 2 kV, a current of 0.17 or 0.34 nA, and a dwell time of 30 µs per pixel were used in serial imaging by the electron beam. The 15-nm-thick layer of the block was milled by focused ion beam at an acceleration voltage of 30 kV and a current of 0.79 nA. All datasets were analyzed using the software IMARIS 8. After *Z* stacks were aligned, 3D mitochondria were manually traced and reconstructed.

Generation of *Aass(R65Q)* and *Aass(G489E)* knock-in mice

C57/B6 mice were used as WT. *Aass(R65Q)* and *Aass(G489E)* knock-in mice were generated by Viewsolid Biotech. Mice were bred onto the C57/B6 background and housed at the animal facility at the Institute of Genetics and Developmental Biology, Chinese Academy of Sciences. All procedures and husbandry were performed according to protocols approved by the Institutional Animal Care and Use Committee at the Institute of Genetics and Developmental Biology, Chinese Academy of Sciences.

Quantitative real-time PCR

RNA was isolated from different tissues of WT (C57/B6) mice using a Multisource Total RNA Miniprep Kit (Axygen). A reverse-transcription kit (Promega) was used to reverse-transcribe RNA in a 20-µl reaction mixture. Quantification of *Aass* gene expression was performed using a real-time PCR system (Bio-Rad) in quadruplicate. *Gapdh* was amplified as the internal control.

Antibodies and Western blot

Antibodies against AASS (1:1,000; HPA020728) and α-tubulin (1:5,000; T6199) were from Sigma-Aldrich. Western blot analysis was performed using liver homogenates. To prepare liver homogenates, 100 mg liver tissue was collected, snap-frozen in liquid nitrogen, homogenized, and ultrasonicated in 400 µl tissue lysis buffer (50 mM Tris-HCl, pH 7.5, 100 mM NaCl, 2 mM EDTA, and 1% NP-40) with protease inhibitor (05892970001; Roche) and phosphatase inhibitor (04906837001; Roche). Liver homogenates were collected from the supernatant after centrifugation at 12,000 *g* at 4°C for 10 min.

Measurements of serum biomarkers

Blood samples collected from P40 mice were incubated on ice for 30 min for coagulation and then centrifuged for 10 min at 3,000 rpm to separate the serum. 50 µl of serum was used for measuring the activity of ALT, AST, CK, LDH, α-HBDH, and CKMB using a 7100 Automatic Biochemical Analyzer (Hitachi High-Technologies). The experiments were not randomized, and no statistical method was used to predetermine sample size. The investigators were not blinded to the group allocation during the experiment and when assessing the outcome.

Hematoxylin-eosin staining

Livers of P40 mice were post-fixed in 4% PFA for 24 h and subsequently subjected to paraffin-embedded sectioning. Briefly, the liver was dehydrated sequentially in graded ethanols (70%, 80%, 95%, 1 h each, followed by 100% alcohol, 1 h three times), and the ethanol was cleared in xylene for 1 h with two repeats. Then the liver was immersed in paraffin for 1 h with three repeats before sectioning on a microtome at 8-µm thickness. The sections were de-paraffinized in xylene for 10 min with three repeats and rehydrated by sequential incubation in graded ethanol (100%, 100%, 95%, 80%, 70%, and 50%, each for 5 min). The sections were then stained with 1× hematoxylin for 18 min, washed with distilled water for 3 s and acid alcohol for 2 s, and then rinsed with distilled water for 14 min. After post-staining with 0.5% eosin for 70 s, the sections were washed with 100% ethanol for 2 min with three repeats and xylene for 2 min with three repeats, and finally mounted for microscopy analysis.

Isolation, culture, and staining of mouse hepatocytes

Hepatocytes were isolated from WT, *Aass(R65Q)*, and *Aass (G489E)* P40 mice. In brief, mouse livers were sequentially perfused with buffer 1 (KRG buffer [k4002; Sigma-Aldrich] with 100 µM EGTA) and buffer 2 (KRG buffer with 0.5 mg/ml collagenase [c5138; Sigma-Aldrich] and 2 mM $CaCl_2$). The livers were then isolated, cut, and filtered to get hepatocytes. The dispersed hepatocytes were cultured at 37°C with 5% CO_2 in DMEM supplemented with 10% FBS and 1% antibiotics. MitoTracker Green (M7514; Invitrogen) staining was performed according to the manufacturers' instructions.

OCR measurement

OCR of hepatocytes were measured in XF media (nonbuffered RPMI 1640 containing 25 mM glucose, 2 mM L-glutamine, and 1 mM sodium pyruvate) under basal conditions and in response to 1 µM oligomycin, 2 µM fluoro-carbonyl cyanide phenylhydrazone, and 1 µM rotenone + 1 µM antimycin A with the XF-24 Extracellular Flux Analyzer (Seahorse Bioscience) following the manufacturers' instructions.

Statistical analysis

Data were analyzed with Prism (GraphPad Software) to generate curves or bar graphs. Error bars represent SEM. The two-tailed unpaired *t* test was used for statistical analysis of two groups of samples. One-way ANOVA with a Newman–Keuls post-test was used to compare the mean differences between multiple groups that have been split on one factor, such as genotype. Two-way ANOVA was used to compare the mean differences between groups that have been split on two independent factors, such as genotype and days aftert L4. For all quantifications, *, $P < 0.05$; **, $P < 0.01$; and ***, $P < 0.001$.

Online supplemental material

Fig. S1 analyzes intracellular organelles, AASS-1 expression pattern, and the levels of saccharopine and lysine in WT and *aass-1* mutants. Fig. S2 describes the generation of *slc-25A29(yq276)*, *aass-1(yq246)*, and *aass-1(yq277)* mutants using CRISPR/Cas9. Fig. S3 analyzes mitochondrial structures in the sheath cells, intestine cells, and muscle cells in N2, *aass-1*, and *fzo-1* animals, intestinal ATP production in N2 and *aass-1* animals, and hypodermal mitochondrial membrane potential and reactive oxygen species production in *aass-1* SDH mutants. Fig. S4 characterizes *Aass* mutant mice. Fig. S5 describes the identification of suppressor genes of the *aass-1(yq170)* mutation. Table S1 lists *C. elegans* expression constructs. Table S2 lists sgRNA targeting sequences and PAM sequences. Videos 1 and 2 show representative 360° views of 3D reconstructed mitochondria in N2 and *aass-1(yq170)* hypodermal cells. Videos 3, 4, and 5 show time-lapse monitoring of mitochondrial dynamics in hypodermal cells in N2 and *aass-1(yq170)* animals. Videos 6 and 7 show time-lapse monitoring of mitochondrial dynamics in hepatocytes of WT and *Aass(G489E)* mice.

Acknowledgments

We thank Drs. Xiaochen Wang, Mengqiu Dong, Hong Zhang, and Shohei Mitani as well as the *C. elegans* Genetic Center for *C. elegans* strains and Dr. I. Hanson for proofreading the manuscript. We thank Drs. Lin Yang and Fang Zhang (Institute of Genetics and Developmental Biology, Chinese Academy of Sciences) for help with TEM, and Drs. Jianguo Zhang and Yun Feng (Center for Biological Imaging, Institute of Biophysics, Chinese Academy of Sciences) for assistance in scanning electron microscope imaging and 3D reconstruction.

W. Guo was funded by the Recruitment Program of the Global Youth Experts of China, 2015. This research was supported by grants from the National Basic Research Program of China (2017YFA0503403), the National Science Foundation of China (31730053 to C. Yang), the Interdisciplinary Innovation Team, Chinese Academy of Sciences (to C. Yang), and the Key Research Program of Frontier Sciences, Chinese Academy of Sciences (QYZDB-SSW-SMC046 to W. Guo).

The authors declare no competing financial interests.

Author contributions: C. Yang, J. Zhou, and W. Guo conceived the study. J. Zhou did most of the experiments. X. Wang contributed to TEM analysis. W. Guo, M. Wang, and Y. Guo contributed to most of the mouse experiments. Y. Chang, F. Zhang, Z. Ban, and G. Wang performed liquid chromatograph–mass spectrometry and analysis. R. Tang, Q. Gan, Q. Zhang, F. Wang, and L. Zhao contributed to EMS screening. W. Qian and S. Wu contributed to the analysis of genome sequence results. Y. Jing contributed to materials. C. Yang, W. Guo, and J. Zhou wrote the manuscript with feedback from all authors.

Submitted: 27 July 2018
Revised: 19 October 2018
Accepted: 15 November 2018

References

Arribere, J.A., R.T. Bell, B.X. Fu, K.L. Artiles, P.S. Hartman, and A.Z. Fire. 2014. Efficient marker-free recovery of custom genetic modifications with CRISPR/Cas9 in *Caenorhabditis elegans*. *Genetics*. 198:837–846. https://doi.org/10.1534/genetics.114.169730

Breckenridge, D.G., B.H. Kang, D. Kokel, S. Mitani, L.A. Staehelin, and D. Xue. 2008. *Caenorhabditis elegans drp-1* and *fis-2* regulate distinct cell-death execution pathways downstream of *ced-3* and independent of *ced-9*. *Mol. Cell*. 31:586–597. https://doi.org/10.1016/j.molcel.2008.07.015

Bruce Alberts, A.J. 2014. Julian Lewis, David Morgan, Martin Raff, Keith Roberts, Peter Walter. Molecular Biology of the Cell. Garland Science, New York.

Carson, N.A., B.G. Scally, D.W. Neill, and L.J. Carré. 1968. Saccharopinuria: a new inborn error of lysine metabolism. *Nature*. 218:679. https://doi.org/10.1038/218679a0

Cederbaum, S.D., K.N.F. Shaw, J. Dancis, J. Hutzler, and J.C. Blaskovics. 1979. Hyperlysinemia with saccharopinuria due to combined lysine-ketoglutarate reductase and saccharopine dehydrogenase deficiencies presenting as cystinuria. *J. Pediatr.* 95:234–238. https://doi.org/10.1016/S0022-3476(79)80657-5

Chen, D., H. Xiao, K. Zhang, B. Wang, Z. Gao, Y. Jian, X. Qi, J. Sun, L. Miao, and C. Yang. 2010. Retromer is required for apoptotic cell clearance by phagocytic receptor recycling. *Science*. 327:1261–1264. https://doi.org/10.1126/science.1184840

Cong, L., F.A. Ran, D. Cox, S. Lin, R. Barretto, N. Habib, P.D. Hsu, X. Wu, W. Jiang, L.A. Marraffini, and F. Zhang. 2013. Multiplex genome engineering using CRISPR/Cas systems. *Science*. 339:819–823. https://doi.org/10.1126/science.1231143

Cox, R.P., P.J. Markovitz, and D.T. Chuang. 1986. Familial hyperlysinemias--multiple enzyme deficiencies associated with the bifunctional aminoadipic semialdehyde synthase. *Trans. Am. Clin. Climatol. Assoc.* 97:69–81.

Dancis, J., J. Hutzler, M.G. Ampola, V.E. Shih, H.H. van Gelderen, L.T. Kirby, and N.C. Woody. 1983. The prognosis of hyperlysinemia: an interim report. *Am. J. Hum. Genet.* 35:438–442.

Davis, M.W., M. Hammarlund, T. Harrach, P. Hullett, S. Olsen, and E.M. Jorgensen. 2005. Rapid single nucleotide polymorphism mapping in *C. elegans. BMC Genomics.* 6:118. https://doi.org/10.1186/1471-2164-6-118

de Wet, J.R., K.V. Wood, M. DeLuca, D.R. Helinski, and S. Subramani. 1987. Firefly luciferase gene: structure and expression in mammalian cells. *Mol. Cell. Biol.* 7:725–737. https://doi.org/10.1128/MCB.7.2.725

Dickinson, D.J., J.D. Ward, D.J. Reiner, and B. Goldstein. 2013. Engineering the *Caenorhabditis elegans* genome using Cas9-triggered homologous recombination. *Nat. Methods.* 10:1028–1034. https://doi.org/10.1038/nmeth.2641

Fiermonte, G., L. Palmieri, S. Todisco, G. Agrimi, F. Palmieri, and J.E. Walker. 2002. Identification of the mitochondrial glutamate transporter. Bacterial expression, reconstitution, functional characterization, and tissue distribution of two human isoforms. *J. Biol. Chem.* 277:19289–19294. https://doi.org/10.1074/jbc.M201572200

Houten, S.M., H. Te Brinke, S. Denis, J.P. Ruiter, A.C. Knegt, J.B. de Klerk, P. Augoustides-Savvopoulou, J. Häberle, M.R. Baumgartner, T. Coşkun, et al. 2013. Genetic basis of hyperlysinemia. *Orphanet J. Rare Dis.* 8:57. https://doi.org/10.1186/1750-1172-8-57

Hudson, R.C., and R.M. Daniel. 1993. L-glutamate dehydrogenases: distribution, properties and mechanism. *Comp. Biochem. Physiol. B.* 106:767–792. https://doi.org/10.1016/0305-0491(93)90031-Y

Ichishita, R., K. Tanaka, Y. Sugiura, T. Sayano, K. Mihara, and T. Oka. 2008. An RNAi screen for mitochondrial proteins required to maintain the morphology of the organelle in *Caenorhabditis elegans. J. Biochem.* 143:449–454. https://doi.org/10.1093/jb/mvm245

Jinek, M., K. Chylinski, I. Fonfara, M. Hauer, J.A. Doudna, and E. Charpentier. 2012. A programmable dual-RNA-guided DNA endonuclease in adaptive bacterial immunity. *Science.* 337:816–821. https://doi.org/10.1126/science.1225829

Kanazawa, T., M.D. Zappaterra, A. Hasegawa, A.P. Wright, E.D. Newman-Smith, K.F. Buttle, K. McDonald, C.A. Mannella, and A.M. van der Bliek. 2008. The C. elegans Opa1 homologue EAT-3 is essential for resistance to free radicals. *PLoS Genet.* 4:e1000022. https://doi.org/10.1371/journal.pgen.1000022

Labrousse, A.M., M.D. Zappaterra, D.A. Rube, and A.M. van der Bliek. 1999. *C. elegans* dynamin-related protein DRP-1 controls severing of the mitochondrial outer membrane. *Mol. Cell.* 4:815–826. https://doi.org/10.1016/S1097-2765(00)80391-3

Lagido, C., J. Pettitt, A.J. Porter, G.I. Paton, and L.A. Glover. 2001. Development and application of bioluminescent Caenorhabditis elegans as multicellular eukaryotic biosensors. *FEBS Lett.* 493:36–39. https://doi.org/10.1016/S0014-5793(01)02271-2

Lagido, C., J. Pettitt, A. Flett, and L.A. Glover. 2008. Bridging the phenotypic gap: real-time assessment of mitochondrial function and metabolism of the nematode *Caenorhabditis elegans. BMC Physiol.* 8:7. https://doi.org/10.1186/1472-6793-8-7

Mali, P., L. Yang, K.M. Esvelt, J. Aach, M. Guell, J.E. DiCarlo, J.E. Norville, and G.M. Church. 2013. RNA-guided human genome engineering via Cas9. *Science.* 339:823–826. https://doi.org/10.1126/science.1232033

Markovitz, P.J., D.T. Chuang, and R.P. Cox. 1984. Familial hyperlysinemias. Purification and characterization of the bifunctional aminoadipic semialdehyde synthase with lysine-ketoglutarate reductase and saccharopine dehydrogenase activities. *J. Biol. Chem.* 259:11643–11646.

Mishra, P., and D.C. Chan. 2016. Metabolic regulation of mitochondrial dynamics. *J. Cell Biol.* 212:379–387. https://doi.org/10.1083/jcb.201511036

Pagliarini, D.J., and J. Rutter. 2013. Hallmarks of a new era in mitochondrial biochemistry. *Genes Dev.* 27:2615–2627. https://doi.org/10.1101/gad.229724.113

Papes, F., E.L. Kemper, G. Cord-Neto, F. Langone, and P. Arruda. 1999. Lysine degradation through the saccharopine pathway in mammals: involvement of both bifunctional and monofunctional lysine-degrading enzymes in mouse. *Biochem. J.* 344:555–563. https://doi.org/10.1042/bj3440555

Pink, D.B., S.K. Gatrell, R. Elango, J. Turchinsky, A.S. Kiess, K.P. Blemings, W.T. Dixon, and R.O. Ball. 2011. Lysine α-ketoglutarate reductase, but not saccharopine dehydrogenase, is subject to substrate inhibition in pig liver. *Nutr. Res.* 31:544–554. https://doi.org/10.1016/j.nutres.2011.06.001

Porcelli, V., G. Fiermonte, A. Longo, and F. Palmieri. 2014. The human gene SLC25A29, of solute carrier family 25, encodes a mitochondrial transporter of basic amino acids. *J. Biol. Chem.* 289:13374–13384. https://doi.org/10.1074/jbc.M114.547448

Sacksteder, K.A., B.J. Biery, J.C. Morrell, B.K. Goodman, B.V. Geisbrecht, R.P. Cox, S.J. Gould, and M.T. Geraghty. 2000. Identification of the alpha-aminoadipic semialdehyde synthase gene, which is defective in familial hyperlysinemia. *Am. J. Hum. Genet.* 66:1736–1743. https://doi.org/10.1086/302919

Shen, E.Z., C.Q. Song, Y. Lin, W.H. Zhang, P.F. Su, W.Y. Liu, P. Zhang, J. Xu, N. Lin, C. Zhan, et al. 2014. Mitoflash frequency in early adulthood predicts lifespan in *Caenorhabditis elegans. Nature.* 508:128–132. https://doi.org/10.1038/nature13012

Simell, O., J.K. Visakorpi, and M. Donner. 1972. Saccharopinuria. *Arch. Dis. Child.* 47:52–55. https://doi.org/10.1136/adc.47.251.52

Vianey-Liaud, C., M.O. Rolland, P. Divry, G. Puthet, M.T. Zabot, and J. Cotte. 1986. A New Case of Hyperlysinaemia with Saccharopinuria. *J. Inherit. Metab. Dis.* 9(S2, Suppl. 2):265–267. https://doi.org/10.1007/BF01799724

Wai, T., and T. Langer. 2016. Mitochondrial Dynamics and Metabolic Regulation. *Trends Endocrinol. Metab.* 27:105–117. https://doi.org/10.1016/j.tem.2015.12.001

Xu, S., and A.D. Chisholm. 2014. *C. elegans* epidermal wounding induces a mitochondrial ROS burst that promotes wound repair. *Dev. Cell.* 31:48–60. https://doi.org/10.1016/j.devcel.2014.08.002

Youle, R.J., and A.M. van der Bliek. 2012. Mitochondrial fission, fusion, and stress. *Science.* 337:1062–1065. https://doi.org/10.1126/science.1219855

Zhang, J., C. Zhao, Y. Chang, Y. Zhao, Q. Li, X. Lu, and G. Xu. 2013. Analysis of free amino acids in flue-cured tobacco leaves using ultra-high performance liquid chromatography with single quadrupole mass spectrometry. *J. Sep. Sci.* 36:2868–2877. https://doi.org/10.1002/jssc.201300450